Coastal Engineering 56 (2009) 1133–1152

Contents lists available at ScienceDirect

Coastal Engineering

journal homepage: www.elsevier.com/locate/coastaleng

Modelling storm impacts on beaches, dunes and barrier islands

Dano Roelvink [a,b,c,*], Ad Reniers [c,d], Ap van Dongeren [b], Jaap van Thiel de Vries [b,c], Robert McCall [b,c], Jamie Lescinski [b]

[a] UNESCO-IHE Institute for Water Education, P.O. BOX 3015, 2601 DA Delft, The Netherlands
[b] Deltares, The Netherlands
[c] Delft University of Technology, The Netherlands
[d] Rosenstiel School of Marine and Atmospheric Science, Univ. of Miami, United States

ARTICLE INFO

Article history:
Received 15 December 2008
Received in revised form 12 July 2009
Accepted 18 August 2009
Available online 15 September 2009

Keywords:
Swash
Low-frequency waves
Dune erosion
Overtopping
Overwashing
Breaching
Morphology
Modelling
XBeach

ABSTRACT

A new nearshore numerical model approach to assess the natural coastal response during time-varying storm and hurricane conditions, including dune erosion, overwash and breaching, is validated with a series of analytical, laboratory and field test cases. Innovations include a non-stationary wave driver with directional spreading to account for wave-group generated surf and swash motions and an avalanching mechanism providing a smooth and robust solution for slumping of sand during dune erosion. The model performs well in different situations including dune erosion, overwash and breaching with specific emphasis on swash dynamics, avalanching and 2DH effects; these situations are all modelled using a standard set of parameter settings. The results show the importance of infragravity waves in extending the reach of the resolved processes to the dune front. The simple approach to account for slumping of the dune face by avalanching makes the model easily applicable in two dimensions and applying the same settings good results are obtained both for dune erosion and breaching.

1. Introduction

The devastating effects of hurricanes on low-lying sandy coasts, especially during the 2004 and 2005 seasons have pointed at an urgent need to be able to assess the vulnerability of coastal areas and (re-)design coastal protection for future events, and also to evaluate the performance of existing coastal protection projects compared to 'do-nothing' scenarios. In view of this the Morphos-3D project was initiated by USACE-ERDC, bringing together models, modelers and data on hurricane winds, storm surges, wave generation and nearshore processes. As part of this initiative an open-source program, XBeach for eXtreme Beach behaviour, has been developed to model the nearshore response to hurricane impacts. The model includes wave breaking, surf and swash zone processes, dune erosion, overwashing and breaching.

Existing tools to assess dune erosion under extreme storm conditions assume alongshore uniform conditions and have been applied successfully along relatively undisturbed coasts (Vellinga, 1986, Steetzel, 1993, Nishi and Kraus, 1996, Larson et al., 2004), but are inadequate to assess the more complex situation where the coast has significant alongshore variability. This variability may result from anthropogenic causes, such as the presence of artificial inlets, sea walls, and revetments, but also from natural causes, such as the variation in dune height along the coast or the presence of rip channels and shoals on the shoreface (Thornton et al., 2007). A particularly complex situation is found when barrier islands protect storm impact on the main land coast. In that case the elevation, width and length of the barrier island, as well as the hydrodynamic conditions (surge level) of the back bay should be taken into account to assess the coastal response. Therefore, the assessment of storm impact in these more complex situations requires a two-dimensional process-based prediction tool, which contains the essential physics of dune erosion and overwash, avalanching, swash motions, infragravity waves and wave groups.

With regard to dune erosion, the development of a scarp and episodic slumping after undercutting is a dominant process (van Gent et al., 2008). This supplies sand to the swash and surf zone that is transported seaward by the backwash motion and by the undertow; without it the upper beach scours down and the dune erosion process slows down considerably. One-dimensional (cross-shore) models such as DUROSTA (Steetzel, 1993) focus on the underwater offshore transport and obtain the supply of sand by extrapolating these transports to the dry dune. Overton and Fisher (1988), Nishi and Kraus (1996) focus on the supply of sand by the dune based on the

* Corresponding author. UNESCO-IHE Institute for Water Education, P.O. BOX 3015, 2601 DA Delft, The Netherlands. Tel.: +31 15 2151838.
E-mail address: d.roelvink@unesco-ihe.org (D. Roelvink).

0378-3839/$ – see front matter © 2009 Elsevier B.V. All rights reserved.
doi:10.1016/j.coastaleng.2009.08.006

concept of wave impact. Both approaches rely on heuristic estimates of the runup and are well suited for 1D application but difficult to apply in a horizontally 2D setting. Hence, a more comprehensive modelling of the swash motions is called for.

Swash motions are up to a large degree a result from wave-group forcing of infragravity waves (Tucker, 1954). Depending on the beach configuration and directional properties of the incident wave spectrum both leaky and trapped infragravity waves contribute to the swash spectrum (Huntley et al., 1981). Raubenheimer and Guza (1996) show that incident band swash is saturated, infragravity swash is not, therefore infragravity swash is dominant in storm conditions. Models range from empirical formulations (e.g. Stockdon et al., 2006) through analytical approaches (Schaeffer, 1994, Erikson et al., 2005) to numerical models in 1D (e.g. List, 1992, Roelvink, 1993b) and 2DH (e.g. van Dongeren et al., 2003, Reniers et al., 2004a, 2006). 2DH wave-group resolving models are well capable of describing low-frequency motions. However, for such a model to be applied for swash, a robust drying/flooding formulation is required.

The objective of this paper is to introduce a model, which includes the above-mentioned physics-based processes and provides a robust and flexible environment in which to test morphological modelling concepts for the case of dune erosion, overwashing and breaching.

In the following we will first discuss the model approach to account for the regimes of dune erosion, overwashing and breaching in Section 2. Section 3 describes the model formulations. This is followed in Section 4 by a series of tests to demonstrate the validity and short-comings of the model with specific emphasis on swash dynamics, avalanching and 2D effects. Discussion and conclusions are presented in Sections 5 respectively.

2. Model approach

Our aim is to model processes in different regimes as described by Sallenger (2000). He defines an Impact Level to denote different regimes of impact on barrier islands by hurricanes, which are the 1) swash regime, 2) collision regime, 3) overwash regime and 4) inundation regime. The approach we follow to model the processes in these regimes is described below.

To resolve the swash dynamics the model employs a novel 2DH description of the wave groups and accompanying infragravity waves over an arbitrary bathymetry (thus including bound, free and refractively trapped infragravity waves). The wave-group forcing is derived from the time-varying wave-action balance e.g. Phillips (1977) with a dissipation model for use in combination with wave groups (Roelvink, 1993a). A roller model (Svendsen, 1984; Nairn et al., 1990; Stive and de Vriend, 1994) is used to represent momentum stored in surface rollers which leads to a shoreward shift in wave forcing.

The wave-group forcing drives infragravity motions and both longshore and cross-shore currents. Wave-current interaction within the wave boundary layer results in an increased wave-averaged bed shear stress acting on the infragravity waves and currents (e.g. Soulsby et al., 1993 and references therein). To account for the randomness of the incident waves the description by Feddersen et al. (2000) is applied which showed good skill for longshore current predictions using a constant drag coefficient (Ruessink et al., 2001).

During the swash and collision regime the mass flux carried by the waves and rollers returns offshore as a return flow or a rip-current. These offshore directed flows keep the erosion process going by removing sand from the slumping dune face. Various models have been proposed for the vertical profile of these currents (see Reniers et al., 2004b for a review). However, the vertical variation is not very strong during extreme conditions and has been neglected for the moment.

Surf and swash zone sediment transport processes are very complex, with sediment stirring by a combination of short-wave and long-wave orbital motion, currents and breaker-induced turbulence. However, intra-wave sediment transports due to wave asymmetry and wave skewness are expected to be relatively minor compared to long-wave and mean current contributions (van Thiel de Vries et al., 2008). This allows for a relatively simple and transparent formulation according to Soulsby–Van Rijn (Soulsby, 1997) in a short-wave averaged but wave-group resolving model of surf zone processes. This formulation has been applied successfully in describing the generation of rip channels (Damgaard et al., 2002 Reniers et al., 2004a) and barrier breaching (Roelvink et al., 2003).

In the collision regime, the transport of sediment from the dry dune face to the wet swash, i.e. slumping or avalanching, is modelled with an avalanching model accounting for the fact that saturated sand moves more easily than dry sand, by introducing both a critical wet slope and dry slope. As a result slumping is predominantly triggered by a combination of infragravity swash runup on the previously dry dune face and the (smaller) critical wet slope.

During the overwash regime the flow is dominated by low-frequency motions on the time scale of wave groups, carrying water over the dunes. This onshore flux of water is an important landward transport process where dune sand is being deposited on the island and within the shallow inshore bay as overwash fans (e.g. Leatherman et al., 1977; Wang and Horwitz, 2007). To account for this landward transport some heuristic approaches exist in 1D, e.g. in the SBeach overwash module (Larson et al., 2004) which cannot be readily applied in 2D. Here, the overwash morphodynamics are taken into account with the wave-group forcing of low-frequency motions in combination with a robust momentum-conserving drying/flooding formulation (Stelling and Duinmeijer, 2003) and concurrent sediment transport and bed-elevation changes.

Breaching of barrier islands occurs during the inundation regime, where a new channel is formed cutting through the island. Visser (1998) presents a semi-empirical approach for breach evolution based on a schematic uniform cross-section. Here a generic description is used where the evolution of the channel is calculated from the sediment transports induced by the dynamic channel flow in combination with avalanche-triggered bank erosion.

3. Model formulations

The model solves coupled 2D horizontal equations for wave propagation, flow, sediment transport and bottom changes, for varying (spectral) wave and flow boundary conditions. Because the model takes into account the variation in wave height in time (long known to surfers) it resolves the long-wave motions created by this variation. This so-called 'surf beat' is responsible for most of the swash waves that actually hit the dune front or overtop it. With this innovation the XBeach model is better able to model the development of the dune erosion profile, to predict when a dune or barrier island will start overwashing and breaching and to model the developments throughout these phases.

3.1. Coordinate system and grid

XBeach uses a coordinate system where the computational x-axis is always oriented towards the coast, approximately perpendicular to the coastline, and the y-axis is alongshore. This coordinate system is defined relative to world coordinates (x_w,y_w) through the origin (x_{ori},y_{ori}) and the orientation alfa, defined counter-clockwise w.r.t. the x_w-axis (East) (Fig. 1).

The grid applied is a rectilinear, non-equidistant, staggered grid, where the bed levels, water levels, water depths and concentrations are defined in cell centers, and velocities and sediment transports are defined in u- and v-points, viz. at the cell interfaces. In the wave energy balance, the energy, roller energy and radiation stress are

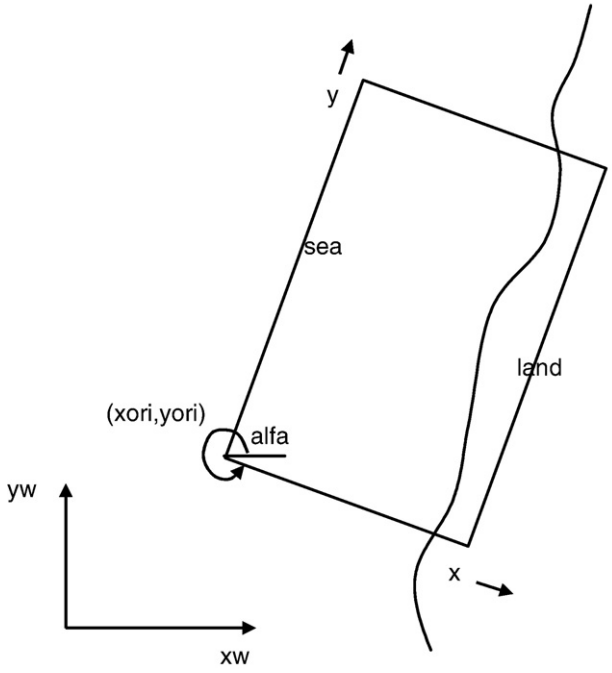

Fig. 1. Coordinate system.

defined at the cell centers, whereas the radiation stress gradients are defined at *u*- and *v*-points.

A first-order upwind explicit scheme with an automatic time step is applied for flow; the discretization is similar to Stelling and Duinmeijer (2003), in the momentum-conserving form, which is especially suitable for drying and flooding and which allows a combination of sub- and supercritical flows. Since the top priority is to provide numerical stability, first-order accuracy is accepted since there is a need for small space steps and time steps anyway, to represent the strong gradients in space and time in the nearshore and swash zone. Because of the many shock-like features in both hydrodynamics and morphodynamics we choose upwind schematizations as a means to avoid numerical oscillations which are otherwise prone to develop in shallow areas.

3.2. Wave-action equation

The wave forcing in the shallow water momentum equation is obtained from a time dependent version of the wave-action balance equation. Similar to Delft University's (stationary) HISWA model (Holthuijsen et al., 1989), the directional distribution of the action density is taken into account whereas the frequency spectrum is represented by a single representative frequency, best represented by the spectral parameter $f_{m,-1,0}$. The wave-action balance is then given by:

$$\frac{\partial A}{\partial t} + \frac{\partial c_x A}{\partial x} + \frac{\partial c_y A}{\partial y} + \frac{\partial c_\theta A}{\partial \theta} = -\frac{D_w}{\sigma} \tag{0.1}$$

with the wave action:

$$A(x,y,t,\theta) = \frac{S_w(x,y,t,\theta)}{\sigma(x,y,t)} \tag{0.2}$$

where θ represents the angle of incidence with respect to the *x*-axis, S_w represents the wave energy density in each directional bin and σ the intrinsic wave frequency. The wave-action propagation speeds in *x*- and *y*-directions are given by:

$$\begin{aligned} c_x(x,y,t,\theta) &= c_g\cos(\theta) + u^L \\ c_y(x,y,t,\theta) &= c_g\sin(\theta) + v^L \end{aligned} \tag{0.3}$$

With u^L and v^L the cross-shore and alongshore depth-averaged Lagrangian velocities respectively (defined below), and the group velocity c_g obtained from linear theory. The propagation speed in θ-space is obtained from:

$$\begin{aligned} c_\theta(x,y,t,\theta) = \frac{\sigma}{\sinh 2kh}\left(\frac{\partial h}{\partial x}\sin\theta - \frac{\partial h}{\partial y}\cos\theta\right) + \cos\theta\left(\sin\theta\frac{\partial u}{\partial x} - \cos\theta\frac{\partial u}{\partial y}\right) \\ + \sin\theta\left(\sin\theta\frac{\partial v}{\partial x} - \cos\theta\frac{\partial v}{\partial y}\right) \end{aligned} \tag{0.4}$$

taking into account bottom refraction (first term on the RHS) and current refraction (last two terms on the RHS) and *h* is the total water depth. The wave number *k* is obtained from the eikonal equations:

$$\begin{aligned} \frac{\partial k_x}{\partial t} + \frac{\partial \omega}{\partial x} &= 0 \\ \frac{\partial k_y}{\partial t} + \frac{\partial \omega}{\partial y} &= 0 \end{aligned} \tag{0.5}$$

where the subscripts refer to the direction of the wave vector components and ω represents the absolute radial frequency. The wave number is then obtained from:

$$k = \sqrt{k_x^2 + k_y^2} \tag{0.6}$$

The absolute radial frequency is given by:

$$\omega = \sigma + k_x u^L + k_y v^L \tag{0.7}$$

and the intrinsic frequency is obtained from the linear dispersion relation.

The total wave energy dissipation, i.e. directionally integrated, due to wave breaking is modelled according to Roelvink (1993a);

$$\begin{aligned} \overline{D}_w &= \frac{\alpha}{\pi} Q_b \sigma E_w \\ Q_b &= 1 - \exp\left(-\left(\frac{H_{rms}}{H_{max}}\right)^n\right),\ H = \sqrt{\frac{8E_w}{\rho g}},\ H_{max} = \frac{\gamma\tanh kh}{k} \end{aligned} \tag{0.8}$$

with $\alpha = O(1)$, ρ the water density, γ the breaker index (a free parameter) and the total wave energy is given by:

$$E_w(x,y,t) = \int_0^{2\pi} S_w(x,y,t,\theta)\,d\theta. \tag{0.9}$$

Next the total wave dissipation, $\overline{D}$, is distributed proportionally over the wave directions:

$$D_w(x,y,t,\theta) = \frac{S_w(x,y,t,\theta)}{E_w(x,y,t)}\,\overline{D}_w(x,y,t) \tag{0.10}$$

This closes the set of equations for the wave-action balance. Given the spatial distribution of the wave action and therefore wave energy the radiation stresses can be evaluated (using linear wave theory):

$$\begin{aligned} S_{xx,w}(x,y,t) &= \int\left(\frac{c_g}{c}(1+\cos^2\theta)-\frac{1}{2}\right)S_w d\theta \\ S_{xy,w}(x,y,t) &= S_{yx,w} = \int \sin\theta\cos\theta\left(\frac{c_g}{c}S_w\right)d\theta \\ S_{yy,w}(x,y,t) &= \int\left(\frac{c_g}{c}(1+\sin^2\theta)-\frac{1}{2}\right)S_w d\theta \end{aligned} \tag{0.11}$$

3.3. Roller energy balance

The roller energy balance is coupled to the wave-action/energy balance where dissipation of wave energy serves as a source term for the roller energy balance. Similar to the wave action the directional distribution of the roller energy is taken into account whereas the frequency spectrum is represented by a single mean frequency. The roller energy balance is then given by:

$$\frac{\partial S_r}{\partial t}+\frac{\partial c_x S_r}{\partial x}+\frac{\partial c_y S_r}{\partial y}+\frac{\partial c_\theta S_r}{\partial \theta} = -D_r + D_w \tag{0.12}$$

with the roller energy in each directional bin represented by $S_r(x,y,t,\theta)$. The roller energy propagation speeds in x- and y-directions are given by:

$$\begin{aligned} c_x(x,y,t,\theta) &= c\cos(\theta)+u^L \\ c_y(x,y,t,\theta) &= c\sin(\theta)+v^L \end{aligned} \tag{0.13}$$

The propagation speed in θ-space is identical to the expression used for the wave energy density propagation (Eq. (0.4)), thus assuming that waves and rollers propagate in the same direction. The phase velocity is obtained from linear wave theory:

$$c = \frac{\sigma}{k} \tag{0.14}$$

The total roller energy dissipation is given by (Reniers et al., 2004a):

$$\overline{D}_r = \frac{2g\beta_r E_r}{c} \tag{0.15}$$

which combines concepts by Deigaard (1993) and Svendsen (1984).

Next the total roller dissipation, $\overline{D}_r$, is distributed proportionally over the wave directions:

$$D_r(x,y,t,\theta) = \frac{S_r(x,y,t,\theta)}{E_r(x,y,t)}\overline{D}_r(x,y,t) \tag{0.16}$$

This closes the set of equations for the roller energy balance.

The roller contribution to radiation stress is given by:

$$\begin{aligned} S_{xx,r}(x,y,t) &= \int\cos^2\theta S_r d\theta \\ S_{xy,r}(x,y,t) &= S_{yx,r}(x,y,t) = \int\sin\theta\cos\theta S_r d\theta \\ S_{yy,r}(x,y,t) &= \int\sin^2\theta S_r d\theta. \end{aligned} \tag{0.17}$$

These roller radiation stress contributions are added to the wave-induced radiation stresses (Eq. (0.11)) to calculate the wave forcing utilizing the radiation stress tensor:

$$\begin{aligned} F_x(x,y,t) &= -\left(\frac{\partial S_{xx,w}+S_{xx,r}}{\partial x}+\frac{\partial S_{xy,w}+S_{xy,r}}{\partial y}\right) \\ F_y(x,y,t) &= -\left(\frac{\partial S_{xy,w}+S_{xy,r}}{\partial x}+\frac{\partial S_{yy,w}+S_{yy,r}}{\partial y}\right). \end{aligned} \tag{0.18}$$

3.4. Shallow water equations

For the low-frequency and mean flows we use the shallow water equations. To account for the wave-induced mass flux and the subsequent (return) flow these are cast into a depth-averaged Generalized Lagrangian Mean (GLM) formulation (Andrews and McIntyre, 1978, Walstra et al., 2000). In such a framework, the momentum and continuity equations are formulated in terms of the Lagrangian velocity, u^L, which is defined as the distance a water particle travels in one wave period, divided by that period. This velocity is related to the Eulerian velocity (the short-wave-averaged velocity observed at a fixed point) by:

$$u^L = u^E + u^S \text{ and } v^L = v^E + v^S. \tag{0.19}$$

Here u^S, v^S represent the Stokes drift in x- and y-directions respectively (Phillips, 1977):

$$u^S = \frac{E_w\cos\theta}{\rho hc} \text{ and } v^S = \frac{E_w\sin\theta}{\rho hc} \tag{0.20}$$

where the wave-group varying short-wave energy and direction are obtained from the wave-action balance (Eq. (0.1)). The resulting GLM-momentum equations are given by:

$$\begin{aligned} &\frac{\partial u^L}{\partial t}+u^L\frac{\partial u^L}{\partial x}+v^L\frac{\partial u^L}{\partial y}-fv^L-\nu_h\left(\frac{\partial^2 u^L}{\partial x^2}+\frac{\partial^2 u^L}{\partial y^2}\right) \\ &\quad = \frac{\tau_{sx}}{\rho h}-\frac{\tau^E_{bx}}{\rho h}-g\frac{\partial\eta}{\partial x}+\frac{F_x}{\rho h} \end{aligned} \tag{0.21}$$

$$\begin{aligned} &\frac{\partial v^L}{\partial t}+u^L\frac{\partial v^L}{\partial x}+v^L\frac{\partial v^L}{\partial y}+fu^L-\nu_h\left(\frac{\partial^2 v^L}{\partial x^2}+\frac{\partial^2 v^L}{\partial y^2}\right) \\ &\quad = +\frac{\tau_{sy}}{\rho h}-\frac{\tau^E_{by}}{\rho h}-g\frac{\partial\eta}{\partial y}+\frac{F_y}{\rho h} \end{aligned} \tag{0.22}$$

$$\frac{\partial\eta}{\partial t}+\frac{\partial hu^L}{\partial x}+\frac{\partial hv^L}{\partial y} = 0. \tag{0.23}$$

Here τ_{bx}, τ_{by} are the bed shear stresses, η is the water level, F_x, F_y are the wave-induced stresses, ν_t is the horizontal viscosity and f is the Coriolis coefficient. The bottom shear stress terms are calculated with the Eulerian velocities as experienced by the bed:

$$u^E = u^L - u^S \text{ and } v^E = v^L - v^S \tag{0.24}$$

and not with the GLM velocities. Also, the boundary condition for the flow computations is expressed in functions of (u^L, v^L) and not (u^E, v^E).

3.5. Sediment transport

The sediment transport is modelled with a depth-averaged advection diffusion equation (Galappatti and Vreugdenhil, 1985):

$$\frac{\partial hC}{\partial t}+\frac{\partial hCu^E}{\partial x}+\frac{\partial hCv^E}{\partial y}+\frac{\partial}{\partial x}\left[D_h h\frac{\partial C}{\partial x}\right]+\frac{\partial}{\partial y}\left[D_h h\frac{\partial C}{\partial y}\right] = \frac{hC_{eq}-hC}{T_s} \tag{0.25}$$

where C represents the depth-averaged sediment concentration which varies on the wave-group time scale, and D_h is the sediment diffusion coefficient. The entrainment of the sediment is represented

by an adaptation time T_s, given by a simple approximation based on the local water depth, h, and sediment fall velocity w_s:

$$T_s = \max\left(0.05\frac{h}{w_s}, 0.2\right)s \tag{0.26}$$

where a small value of T_s corresponds to nearly instantaneous sediment response. The entrainment or deposition of sediment is determined by the mismatch between the actual sediment concentration, C, and the equilibrium concentration, C_{eq}, thus representing the source term in the sediment transport equation.

The bed-updating is discussed next. Based on the gradients in the sediment transport the bed level changes according to:

$$\frac{\partial z_b}{\partial t} + \frac{f_{mor}}{(1-p)}\left(\frac{\partial q_x}{\partial x} + \frac{\partial q_y}{\partial y}\right) = 0 \tag{0.27}$$

where p is the porosity, f_{mor} is a morphological acceleration factor of O (1–10) (e.g. Reniers et al., 2004a) and q_x and q_y represent the sediment transport rates in x- and y-directions respectively, given by:

$$q_x(x,y,t) = \left[\frac{\partial hCu^E}{\partial x}\right] + \left[\frac{\partial}{\partial x}\left[D_h h\frac{\partial C}{\partial x}\right]\right] \tag{0.28}$$

and

$$q_y(x,y,t) = \left[\frac{\partial hCv^E}{\partial y}\right] + \left[\frac{\partial}{\partial y}\left[D_h h\frac{\partial C}{\partial y}\right]\right]. \tag{0.29}$$

3.6. Transport formulations

The equilibrium sediment concentration can be calculated with various sediment transport formulae. At the moment the sediment transport formulation of Soulsby–van Rijn (Soulsby, 1997) has been implemented. The C_{eq} is then given by:

$$C_{eq} = \frac{A_{sb} + A_{ss}}{h}\left(\left(|u^E|^2 + 0.018\frac{u_{rms}^2}{C_d}\right)^{0.5} - u_{cr}\right)^{2.4}(1-\alpha_b m) \tag{0.30}$$

where sediment is stirred by the Eulerian mean and infragravity velocity in combination with the near bed short-wave orbital velocity, u_{rms}, obtained from the wave-group varying wave energy using linear wave theory. The combined mean/infragravity and orbital velocity have to exceed a threshold value, u_{cr}, before sediment is set in motion. The drag coefficient, C_d, is due to flow velocity only (ignoring short-wave effects). To account for bed-slope effects on the equilibrium sediment concentration a bed-slope correction factor is introduced, where the bed slope is denoted by m and α_b represents a calibration factor. The bed load coefficients A_{sb} and the suspended load coefficient A_{ss} are functions of the sediment grain size, relative density of the sediment and the local water depth (see Soulsby, 1997 for details).

3.7. Avalanching

To account for the slumping of sandy material during storm-induced dune erosion avalanching is introduced to update the bed evolution. Avalanching is introduced when a critical bed slope is exceeded:

$$\left|\frac{\partial z_b}{\partial x}\right| > m_{cr} \tag{0.31}$$

with a similar expression for the y-direction. Here we consider that inundated areas are much more prone to slumping and therefore we apply separate critical slopes for dry and wet points; default values are 1 and 0.3, respectively. The former value is consistent with the equilibrium profile according to Vellinga (1986); it is higher than the angle of natural repose and must be seen as an average slope observed after dune erosion, where some stretches may exhibit vertical slopes and other, drier parts may have slumped further. The underwater critical slope is much lower, and our estimate is based on the maximum underwater slopes we have observed in experiments, e.g. the Zwin test (see below) and tests carried out at Oregon State University with initially rather steep profiles.

When the critical slope between two adjacent grid cells is exceeded, sediment is exchanged between these cells to the amount needed to bring the slope back to the critical slope. This exchange rate is limited by a user-specified maximum avalanching transport rate, which for sandy environments is usually set so high as to have no influence on the outcome, while ensuring numerical stability.

In our model simulations, the avalanching mechanism is typically triggered when a high infragravity wave reaches the dune front and partly inundates it. The critical underwater slope is suddenly exceeded and the two grid cells at the dune foot are adjusted during the first timestep when this happens. In subsequent timesteps a chain reaction may take place both in points landward, where now the critical dry slope may be exceeded because of the lowering of the last wet point, and in points seaward, where now the critical wet slope may be exceeded. As a result, sediment is brought from the dry dune into the wet profile, where it is transported further seaward by undertow and infragravity backwash. An essential difference with similar procedures in other dune erosion models is the fact that avalanching is only applied between adjacent grid cells, rather than extrapolating profile behaviour well beyond the wet domain. This is made possible by explicitly resolving the long-wave swash motions. Another big advantage with respect to existing procedures is that the simple avalanching algorithm is readily applied in two dimensions.

3.8. Wave boundary conditions

For the waves the wave energy density at the offshore boundary is prescribed as a function of y, θ and time. This can be generated for given spectral parameters or using directional spectrum information. The method is based on the theory of Hasselmann (1962) (c.f. Herbers et al., 1994), previously implemented and used by Van Dongeren et al. (2003) to model infragravity waves in the nearshore. At the lateral boundaries, for wave components entering the domain, the alongshore or along-crest gradient is set to zero, effectively eliminating the notorious 'shadow zones' found in many wave models.

3.9. Flow boundary conditions

At the seaward and landward (in case of a bay) boundary radiating boundary conditions are prescribed, taking into account the incoming bound long waves, following Van Dongeren and Svendsen (1997a).

For the lateral boundaries so-called Neumann boundaries are used, where the longshore water level gradient is prescribed, in this case set to zero. This type of boundary conditions has been shown to work quite well with (quasi-)stationary situations, where the coast can be assumed to be uniform alongshore outside the model domain. So far we have found that also in case of obliquely incident wave groups this kind of boundary conditions appears to give no large disturbances, although it takes some alongshore distance for edge waves and shear waves to be fully developed.

4. Model verification cases

To verify the implementation and validate the model approach described in Section 3 a number of test cases have been carried out, both in 1D and in 2DH mode. The first series of tests focuses on the description of the wave-group induced hydrodynamics, swash

dynamics, sediment transports and concurrent bed evolution in a one-dimensional setting. Tests include both laboratory and field cases to examine the general validity of the modelling with emphasis on both swash dynamics and avalanching. Next a number of tests are performed including the alongshore dimension. These 2D mode tests include analytical and field cases with alongshore variability in the forcing and/or the bathymetry. All tests have been performed with a standard set of parameter settings (see Appendix A) unless stated otherwise. In addition, for all tests the model performance was quantified by determining error parameters for the modelled hydrodynamics and morphodynamics, which are listed in Table 1.

The model validation commences with 1D large-scale dune erosion test (Arcilla et al., 1994), validating short-wave and long-wave motions as well as the sediment transport and profile evolution in well-controlled conditions. Next a more recent test with combined dune erosion and overtopping is examined (van Gent et al., 2008) showing again that inner surf hydrodynamics, sediment transports and profile evolution are well represented. This is followed by a series of field-scale tests of dune erosion and overwashing on different profiles that are compared with observations reported by Jiménez et al. (2006) after Assateague Island was hit by two northeasters in 1998. Next a number of tests are performed including the alongshore dimension. Starting with a two-dimensional case of long-wave runup (Zelt, 1986), followed by comparisons with field measurements at Duck, NC during the Delilah field experiment to show the ability of the model to capture two-dimensional hydrodynamic processes on a real beach. Finally the process of breaching is tested against a prototype field experiment reported by Visser (1998).

4.1. LIP11D delta flume 1993—test 2E

This model test, described in Arcilla et al. (1994), concerns extreme conditions with a raised water level at 4.58 m above the flume bottom, a significant wave height, H_{m0}, of 1.4 m and peak period, T_p, of 5 s. Bed material consisted of sand with a D_{50} of approximately 0.2 mm. During the test substantial dune erosion took place.

Based on the integral wave parameters H_{m0} and T_p and a standard Jonswap spectral shape, time series of wave energy were generated and imposed as boundary condition. Since the flume tests were carried out with first-order wave generation (no imposed super-harmonics and sub-harmonics), the hindcast runs were carried out with the incoming bound long waves set to zero ('first-order wave generation'). Active wave reflection compensation was applied in the physical model, which has a result similar to the weakly reflective boundary condition in XBeach, namely to prevent re-reflecting of outgoing waves at the wave paddle (offshore boundary).

A grid resolution of 1 m was applied and the sediment transport settings were set at default values, see Appendix A. For the morphodynamic testing the model was run for 0.8 h of hydrodynamic time with a morphological factor of 10, effectively representing a morphological simulation time of 8 h.

Test results are given for the root mean square wave height, H_{rms}, and the root mean square orbital velocity, U_{rms}, separated in high-frequency (frequencies above $f_p/2$ corresponding to incident waves) and low-frequency parts (corresponding to infragravity waves). In XBeach model terms, these parameters are defined as follows:

$$H_{rms,HI} = \sqrt{< H^2 >} \tag{0.32}$$

$$u_{rms,HI} = \sqrt{< u_{rms}^2 >},\ u_{rms} = \frac{1}{\sqrt{2}} \frac{\pi H}{T_p \sinh(kh)} \tag{0.33}$$

$$H_{rms,LO} = \sqrt{8 < (\eta - < \eta >)^2 >} \tag{0.34}$$

$$u_{rms,LO} = \sqrt{< (u^L - < u^L >)^2 >}. \tag{0.35}$$

In Fig. 2 the results are shown both for first-order wave generation (as in the flume tests) and for second-order wave generation (including incoming bound long waves). The model is clearly capable of capturing both the HF and LF wave heights and orbital velocities; it also shows the effect of second-order wave generation on the LF waves. For this test, the agreement is indeed better if incoming bound long waves are omitted from the flow boundary condition (as they were in the laboratory test).

In Fig. 3 the horizontal distribution of sedimentation and erosion after 8 h is shown, and the evolution in time of the erosion volume and the dune retreat, again both for first-order wave generation (as in the physical test) and for second-order steering. For the correct steering, we see a good agreement for all three parameters. Noteworthy is the episodic behaviour of the dune erosion, both in measurements and model, although the almost exact (deterministic) reproduction of the (stochastic) dune retreat must be a coincidence. An important conclusion for physical model tests is that for dune erosion it does make a difference whether first-order or second-order wave steering is applied.

A key element in the modelling is the avalanching algorithm; even though surfbeat waves running up and down the upper beach are fully resolved by the model, without a mechanism to transport sand from the dry dune face to the beach the dune face erosion rate is substantially underestimated. The relatively simple avalanching algorithm described above, whereby an underwater critical slope of 0.3 and a critical slope above water of 1.0 are applied, proves to be quite successful in representing the retreat of the upper beach and dune face. In Fig. 4 the measured and modelled bed evolution are shown, which looks quite good in the upper region. In contrast, Fig. 5 shows the results of two simulations where either the avalanching mechanism (left panel) or the infragravity wave motion (right panel) were left out. Both cases show significant underprediction of the dune erosion, which demonstrates the need to have both processes included in the model.

Error statistics for the standard run are collected in Table 5, and generally show a scatter index and relative bias of less than 10% for

Table 1
Definition of error parameters.

Parameter	Formula (m = measured, c = computed)	Remarks
Correlation coefficient R^2	$\frac{Cov(m,c)}{\sigma_m \sigma_c}$	$R^2 = 1$ means no scatter, tendency may still be wrong
Scatter index SCI	$\frac{rms_{c-m}}{\max(rms_m, \lvert <m> \rvert)}$	This is a relative measure of the scatter between model and data. The error is normalized with the maximum of the rms of the data and the absolute value of the mean of the data; this avoids strange results for data with small mean and large variability
Relative bias	$\frac{< c-m >}{\max(rms_m, \lvert < m > \rvert)}$	This is a relative measure of the bias, normalized in the same way as the Scatter Index.
Brier Skill Score BSS	$1 - \frac{Var(c-m)}{Var(m)}$	This parameter relates the variance of the difference between data and model to the variance of the data. BSS = 1 means perfect skill, BSS = 0 means no skill, BSS < 0 means model is worse than 'no change' scenario. We consider this parameter mainly to judge the skill of the sedimentation/erosion patterns

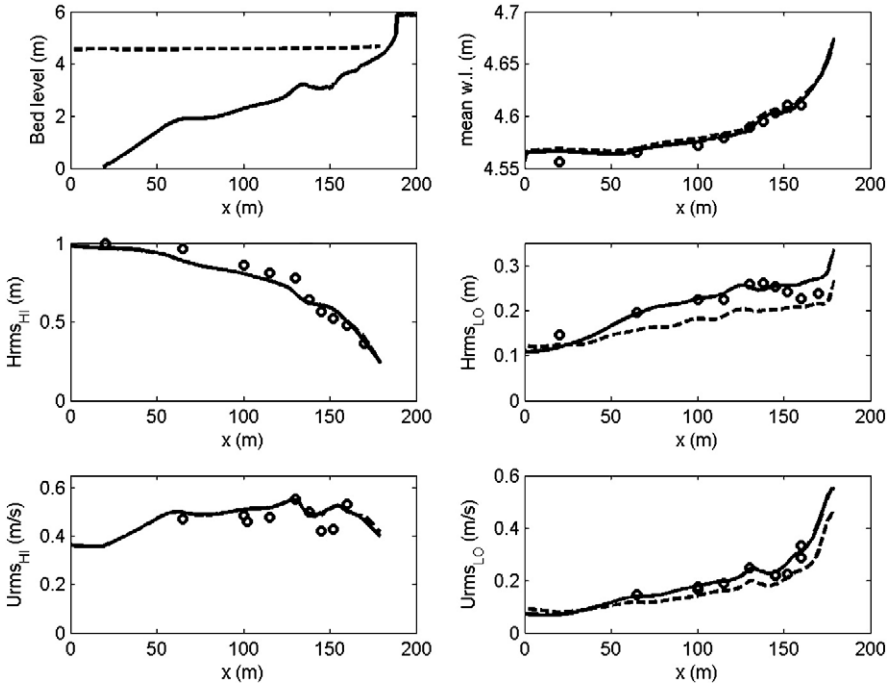

Fig. 2. Computed and observed hydrodynamic parameters for test 2E of the LIP11D experiment. Top left: bed level and mean water level. Top right: measured (dots) and computed mean water level with first-order steering (drawn line) and second-order steering (dashed line) as a function of the cross-shore distance. Middle left: same for HF wave height; middle right: same for LF wave height; bottom left: same for HF orbital velocity; bottom right: same for LF orbital velocity.

the hydrodynamic parameters and overall erosion volumes and dune retreat. An exception is the mean velocity, for which the higher scatter and bias can be attributed to the (neglected) 3D structure of this parameter. The horizontal distribution of the sedimentation and erosion at the end of the test shows a higher scatter, determined in part by the areas with small changes; the Brier Skill Score shows a value of 0.72, which for morphodynamic models is considered good (Van Rijn et al., 2003).

4.2. Deltaflume 2006

We continue with a more recent test of a more complex profile (van Gent et al., 2008, test T4) in which a small dune in front of a large volume dune is breached (see Fig. 6). In addition, a sand mining pit is present in the profile at $x = 65$ m, which is believed to have little influence on the nearshore dynamics and the amount of dune erosion. This test is the best controlled case with dune overwash known to us.

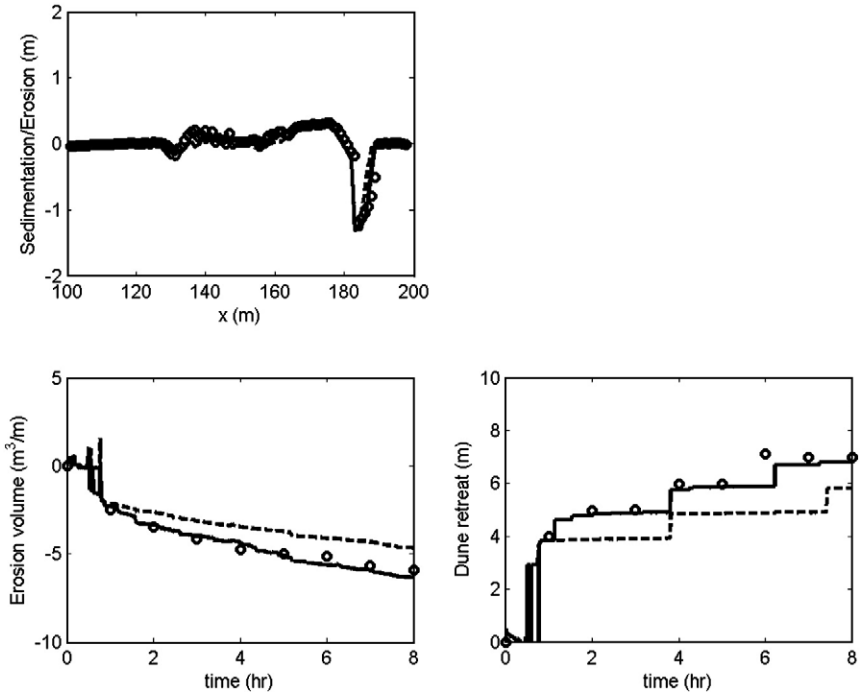

Fig. 3. Computed and observed sedimentation and erosion after 8 hrs (top panel); erosion volume as function of time (bottom left) and dune retreat (bottom right) as function of time for test 2E of the LIP11D experiment, (Arcilla et al., 1994). All results with first-order steering (drawn line) and second-order steering (dashed line).

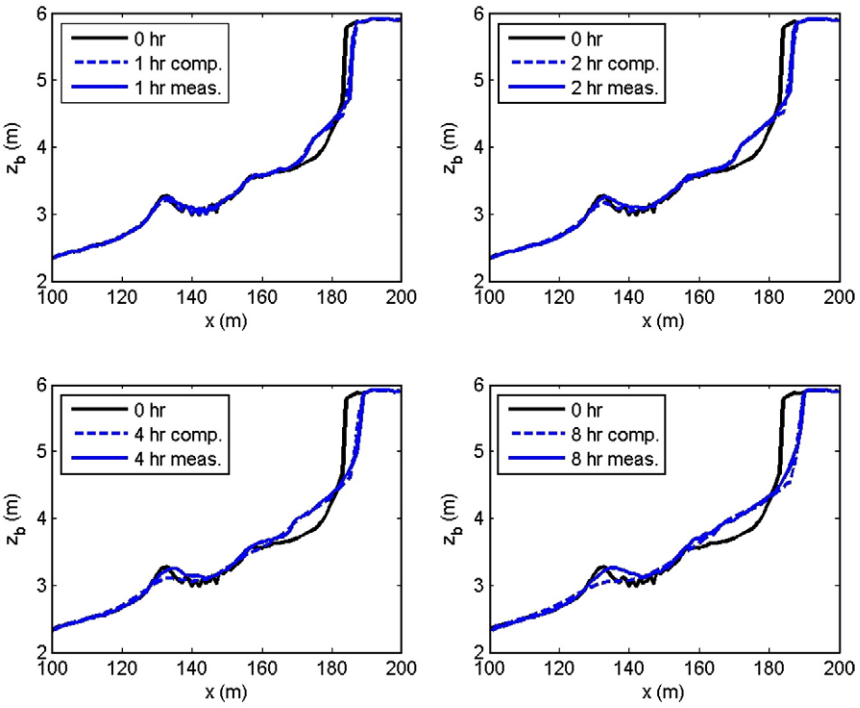

Fig. 4. Measured and modelled bed level after 1, 2, 4 and 8 h of wave action, for a water level of 4.56 m above the flume bottom.

The test duration is 6 h and profile measurements were obtained after 0.l, 0.3, 1.0, 2.0 and 6.0 h. Also detailed measurements of wave transformation, near dune flows and sediment concentrations are available for comparing with model results. In the physical model test the still water level was set at 4.5 m above the flume's floor and imposed wave conditions correspond to a Pierson–Moskowitz spectrum with $H_{m0} = 1.5$ m and $T_p = 4.90$ s. The wave paddle was operated with active wave reflection and second-order steering. Further details may be found in Van Gent et al., 2008 and Van Thiel de Vries et al., 2008.

The simulation is performed for 6 h on a uniform grid in which the grid size Δx is set at 1 m. In order to make a detailed comparison between measured and simulated hydrodynamics over the developing profile, the simulation is carried out with a morphological factor of 1. The offshore model boundary is located at 41 m from the wave board and we use measured water surface elevations and flow velocities at this location to obtain time series of the incident wave energy and the incoming bound long-wave water surface elevations. Other model settings are the same as for test 2E of the LIP11D experiment and are listed in Appendix A.

Fig. 6 compares the modelled and observed profile evolution. Both model and data first show a scarping of the profile, a brief period of overwashing followed by a smoothing out of the remainder of the berm and a renewed attack on the actual dune face, which is slow as most of the wave energy dissipates on the shallow upper profile left by the berm. The modelled profile evolution appears to be slightly slower than observed and also at the end of the test the modelled upper profile is slightly too low, which could be due to lack of onshore sediment transports.

Test averaged hydrodynamic parameters are compared in Fig. 7 and reveal a good agreement between measured and simulated wave height transformation for both incident and long waves (upper left panel), the wave orbital flows for both incident and long waves (upper right panel) and the time and depth-averaged return flow (lower right panel). It is remarked that the measured time and depth-averaged flows just in front of the dune (at $x = 205$ m) should be interpreted with care since in the physical model only limited observation points over depth are available (Van Thiel de Vries et al., 2008).

Error statistics are collected in Table 5, and generally show a scatter index and relative bias of less than 10% for the hydrodynamic parameters and overall erosion volumes and dune retreat. An exception is the mean velocity, for which the higher scatter and bias can be attributed to the (neglected) 3D structure of this parameter. The horizontal distribution of the sedimentation and erosion at the end of the test shows a bit higher scatter, determined in part by the areas with small changes; the Brier Skill Score shows a value of 0.98.

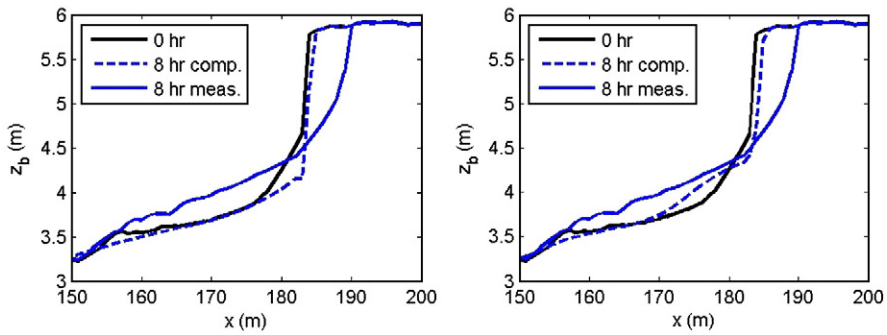

Fig. 5. Measured (drawn line) and modelled (dashed line) profile after 8 h of wave action, left panel: no avalanching; right panel: no wave groups.

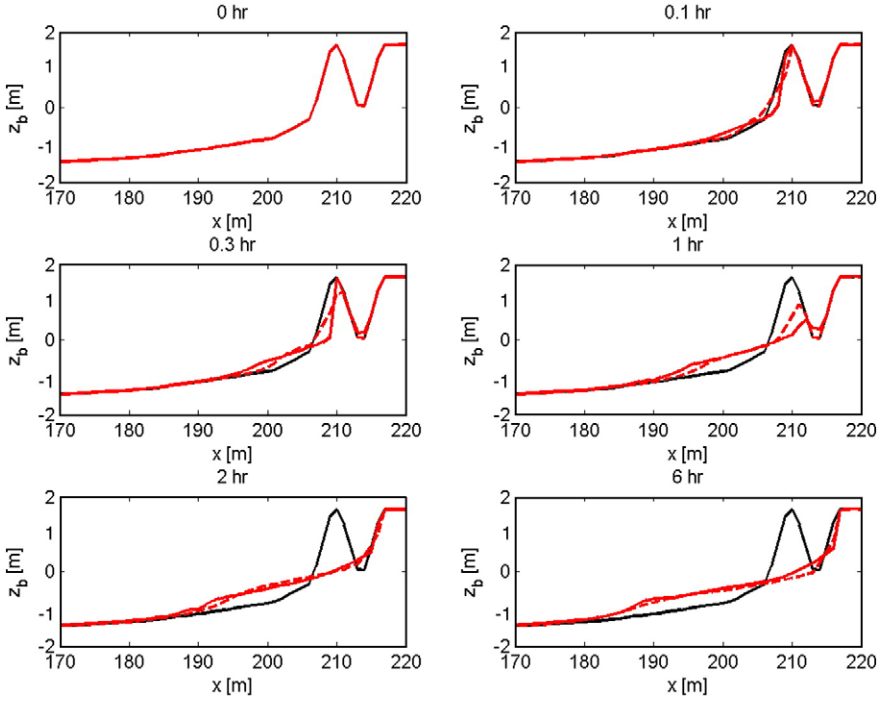

Fig. 6. Deltaflume 2006 test T04. Measured (drawn lines) and modelled (dashed lines) profile after 0, 0.1, 0.3, 1, 2 and 6 h of wave action.

A more detailed analysis of the hydrodynamics is given in Figs. 8 and 9 which compare measured and simulated wave spectra and water surface elevation time series respectively. It is remarked that the measured wave spectra and water surface elevations include both the incident waves and long waves whereas the simulation results are associated with (wave-group generated) long waves only. Considering the wave spectra first, it is seen that the measured wave spectra show a shift in variance towards lower frequencies as the waves propagate to the dune face. At the offshore model boundary most of the measured wave variance is associated with incident waves and the simulated long-wave spectrum explains a marginal part of the measured wave spectrum. However, getting close to the dune face the incident wave variance reduces due to depth induced breaking whereas the long-wave variance increases due to shoaling (Battjes et al., 2004). At the most shoreward pressure sensor (about 10 m from the dune face) most of the measured wave variance is associated with long waves and is favourably simulated with the surfbeat model. The same phenomenon can be observed in Fig. 9, which shows a reasonably good correlation

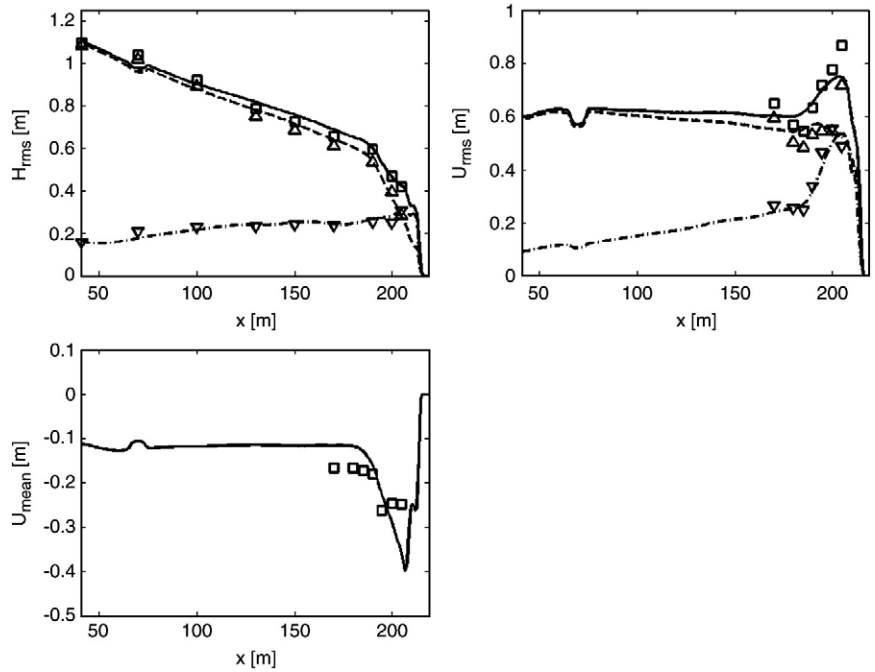

Fig. 7. Deltaflume 2006 test T04. Upper left panel: measured (markers) and simulated (lines) LF (downward triangles/dashed–dotted line), HF (upward triangles/dashed line) and total (squares/solid line) wave height. Upper right panel: measured (markers) and simulated (lines) orbital flow velocity. Lower left panel: measured (squares) and simulated (solid line) time and depth-averaged flow velocity.

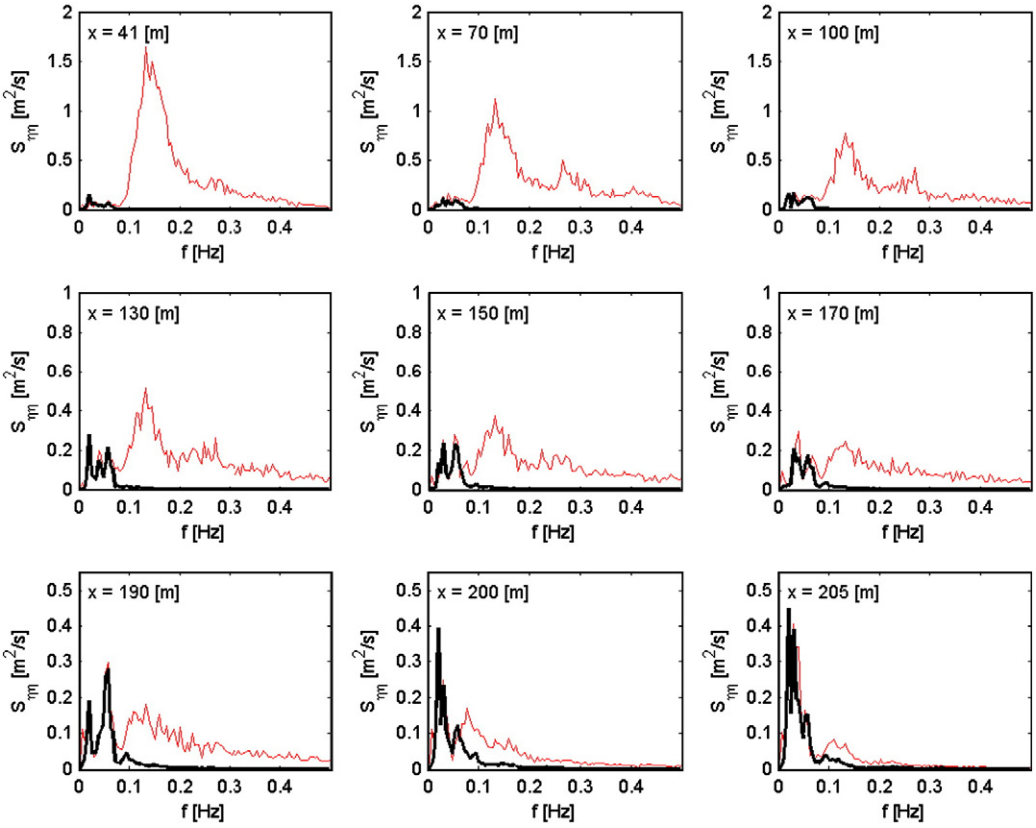

Fig. 8. Measured wave spectra including both incident waves and long waves (thin line) compared with simulated long-wave spectra (thick line) at different cross-shore positions (see upper left corner of sub-panels). Measured and simulated spectra are computed over the whole test duration.

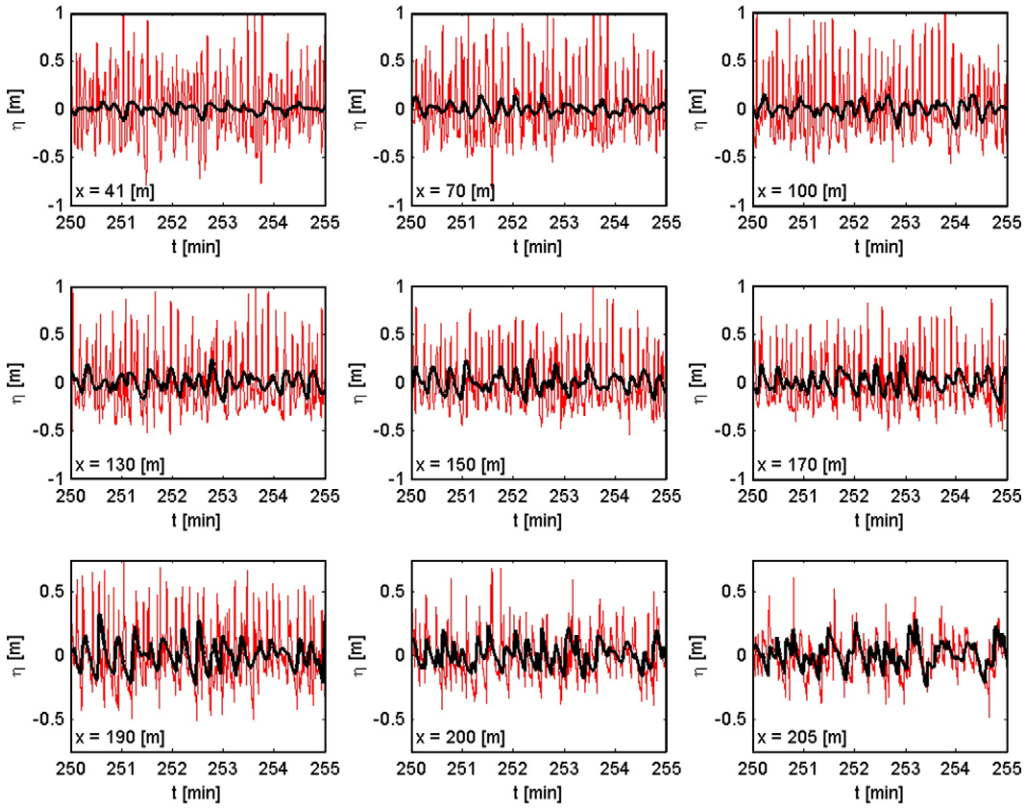

Fig. 9. Measured water surface elevations including both incident and long waves (thin line) compared with simulated long-wave water surface elevations (thick line) at different cross-shore positions (see lower left corner of sub-panels) after 4.17 wave hours.

($R^2 = 0.32$) between measured and simulated water surface elevations close to the dune face (lower right panel). Also the time series show steep long-wave fronts indicating breaking as was shown in the bichromatic wave case by Van Dongeren et al. (2007).

A comparison given between the observed and modelled sediment concentrations and sediment transports (Fig. 10) shows that the model clearly underestimates the concentration near the dune face, whereas the sediment transport is somewhat overestimated. The explanation for this could be found in an overestimation of the near dune time and depth-averaged undertow which compensates for underestimating the near dune sediment concentrations. Throughout the flume, the sediment transport is too much seaward, as no onshore processes are included yet; work to improve this is currently underway but beyond the scope of this paper. Simulated sediment transport *gradients* are favourably predicted by the model, which results in a response of the coastal profile that compares reasonably well to the measurements.

4.3. Dune erosion and overwash field tests

Besides well-controlled laboratory cases, the model is also applied to the field. The first example concerns the morphodynamic response of sandy dunes to extreme storm impacts at Assateague Island, Maryland, USA, which was analyzed before by Jiménez et al. (2006). Two consecutive northeasters attacked the barrier island during late January and early February, 1998. The bathymetry was measured using LIDAR in September 1997 and again February 9th and 10th, 1998 after the two storms had subsided.

Three types of dunes were identified by Jiménez et al. (2006), shown in Fig. 11. Profile A (upper left panel) is initially characterized by a steep faced dune, where the maximum runup exceeded the dune crest height and the mildly sloped back of the dune. The morphological response is characterized by profile lowering, decrease of the beach face slope and landward barrier displacement, while retaining barrier width.

Profile type B is a double-peaked dune profile and has two different shapes. Profile B1 (upper right panel) is initially characterized by a primary and secondary dune, both of which are lower than the maximum runup height and which are separated by a valley. Profile B2 (bottom left panel) initially has two peaks of which the seaward one is lower. The backside of the barrier of either type is therefore either characterized by a secondary dune line (profile B1) or a taller crest of the dune (profile B2) which prevents the eroded sand from being transported to the backside of the dune. The main morphological response for these profile types is a decrease of the beach face slope, outer shoreline retreat and narrowing of the barrier.

The height of the dune crest of profile C (lower right panel) exceeds the maximum runup height and so little overwash is observed. The morphological response of this type of profile is crest lowering due to slumping, decrease of the beach face slope and retreat of the outer shoreline. The width of the barrier is seen to decrease.

The storm impact of the two North Easters on Assateague Island was modelled with XBeach for the four profiles described by Jiménez et al. (2006). The profiles were extended with a shallow foreshore and a 1:100 slope in seaward direction till a water depth of 9 m below NAVD88. As XBeach has not been shown to accurately simulate morphological change during very long storm durations, the simulations were run for a total of 20 h. The measured wave and surge conditions were parameterized for each storm by a constant surge level and a constant wave height and wave period (see Table 2). This approach assumes that two 72 hour storms with varying surge and wave conditions can be approximated by two 10 hour simulations with constant maximum surge and wave conditions following a similar approach as Vellinga (1986). This approach also facilitates further sensitivity studies into the effect of varying hydraulic forcing conditions. The calculation grid size varies from 18 m at the offshore boundary to 2 m on the islands. A morphological acceleration factor of 5 is applied. The final simulated bed profiles are shown in Fig. 11.

The profile changes calculated by XBeach are largely consistent with the description of dune evolution given by Jiménez et al. (2006). Jiménez et al. observed that profile A became flatter, with large quantities of eroded sediment deposited on the back side of the barrier island, due to the consistent wave overtopping. The model replicates this behaviour, except that the island is lowered more than in the measurements and that the seaward face of the island does not roll back as it does in the measurements.

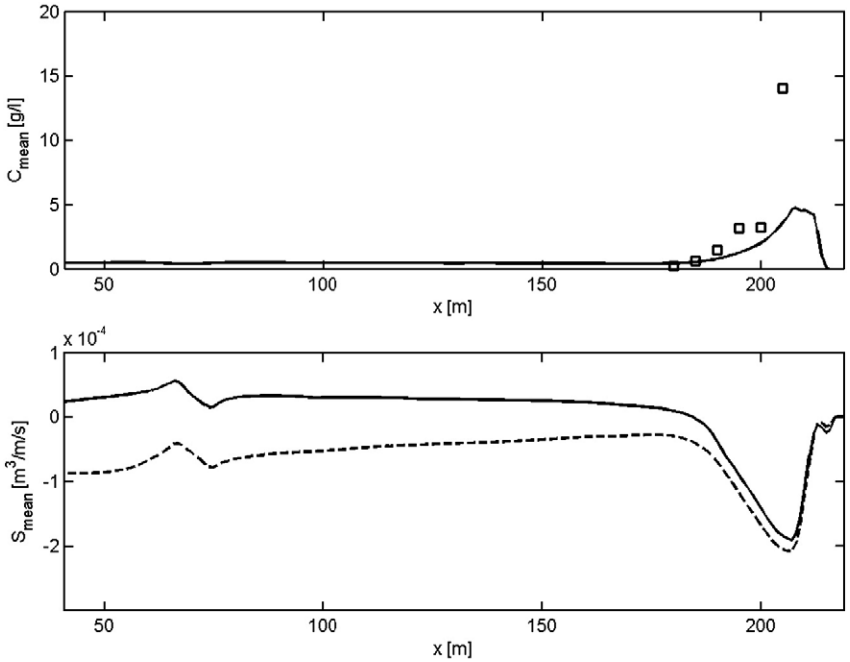

Fig. 10. Deltaflume 2006. Test T04. Top panel: observed depth-averaged concentrations (squares) vs. model result. Bottom panel: total sediment transport observed from profile evolution (drawn line) vs. model result (dashed line).

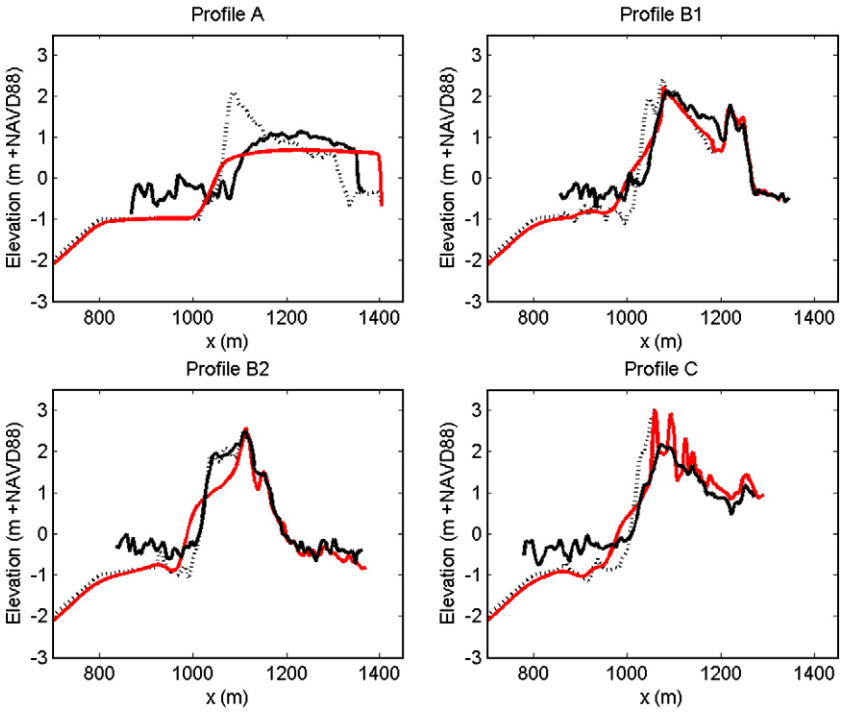

Fig. 11. Pre-storm profiles (black dotted line), measured post-storm profiles (black solid line) and modelled post-storm profiles (red solid line). Upper left panel: profile A. Upper right panel: profile B1. Lower left panel: profile B2. Lower right panel: profile C. The seaward side is on the left of all panels. Note that the measured post-storm profiles contain only the sea surface and emerged topography and no submerged topography.

The observed response of profile B1 was dune face retreat, overwash deposition in the dune valley between the primary and secondary dunes and narrowing of the island, Jiménez et al. (2006) also noted decrease of the beach face slope. It can be seen in Fig. 11 that the morphological development of the island is well represented by the model. The simulated dune crest retreat corresponds closely to the measured retreat. Overwash takes place in the model and sediment is deposited in the valley between the primary and secondary dunes, although the magnitude of deposition is less than in the measurements.

The XBeach model of profile B2 shows a slope reduction on the seaward side and lowering of the seaward dune. The second dune crest retains its crest level as described in the work of Jiménez et al. (2006). The beach slope decrease in the XBeach model is in line with the description given by Jiménez et al. (2006), but differs from their measured profile. It is unclear why the measured profile shows almost no erosion of the beach face.

Jiménez et al. (2006) observed, in general, profile C to lower in height, the seaward dune slope to become smaller, and seaside retreat of the shoreline resulting in barrier narrowing. The XBeach model shows retreat of the upper dune face and a reduction of the seaward dune slope. The model overpredicts the sedimentation at the base of the dune and underpredicts the crest lowering.

Though the model reasonably predicts post-storm beach and dune topography the results are obtained from a model that is based on several simplifications according to surge and wave conditions. In addition the underwater profile is unknown at the seaside and is schematized with a 1:100 slope. A quantitative comparison of modelled and measured profile evolution therefore has limited validity; however we can conclude that the model has qualitative skill in predicting overwash morphology.

In order to obtain more insight in the effect of these simplifications and assumptions on the morphological response during the storms, additional simulations were performed with varying surge levels, wave conditions and foreshore slopes as listed in Table 3.

The sensitivity studies show that the variation in the morphological response of the profiles to the incident wave parameters and surge level is dependent on the initial shape of the profile. This sensitivity is most prominent in profile A (Fig. 12), in which overwash occurs for much of the storm duration, and least in profile C (Fig. 13), in which only dune erosion takes place. This shows that more accurate hydraulic boundary conditions are required in order to correctly simulate field cases with overwash than cases with dune erosion. The parameterization of the hydraulic boundary conditions in this study follows an approach designed for dune erosion cases (Vellinga, 1986). The sensitivity cases suggest that this approach may not be applicable to overwash cases. Further research into storm schematisation for overwash conditions is needed before the model can be considered more than qualitatively correct for overwash.

Table 2
Hydrodynamic boundary conditions XBeach simulations.

	Storm 1	Storm 2
Surge level [m] + NAVD	0.75	1.0
H_s [m]	4.1	3.9
T_p [s]	8.5	8.5
Spectrum	Pierson–Moskowitz	Pierson–Moskowitz

4.4. Zelt analytical 2DH runup case

All the verification cases so far considered solely the cross-shore dimension and assumed a longshore uniform coast. In the following cases the potential of the model to predict coastal and dune erosion in situations that include the 2 horizontal dimensions is further examined. A first step towards a 2DH response is to verify that the 2DH forcing by surge runup and rundown is accurately modelled. This accuracy is controlled by the flooding and drying criterion. This criterion is tested against a numerical solution for the runup of a

Table 3
Sensitivity cases.

	Base	S1	S2	S3	S4	S5	S6	S7	S8
Surge level [m] + NAVD (%)	100	125	75	100	100	100	100	100	100
H_s [m] (%)	100	100	100	125	75	100	100	100	100
T_p [s] (%)	100	100	100	100	100	125	75	100	100
Foreshore slope	0.01	0.01	0.01	0.01	0.01	0.01	0.01	0.02	0.005

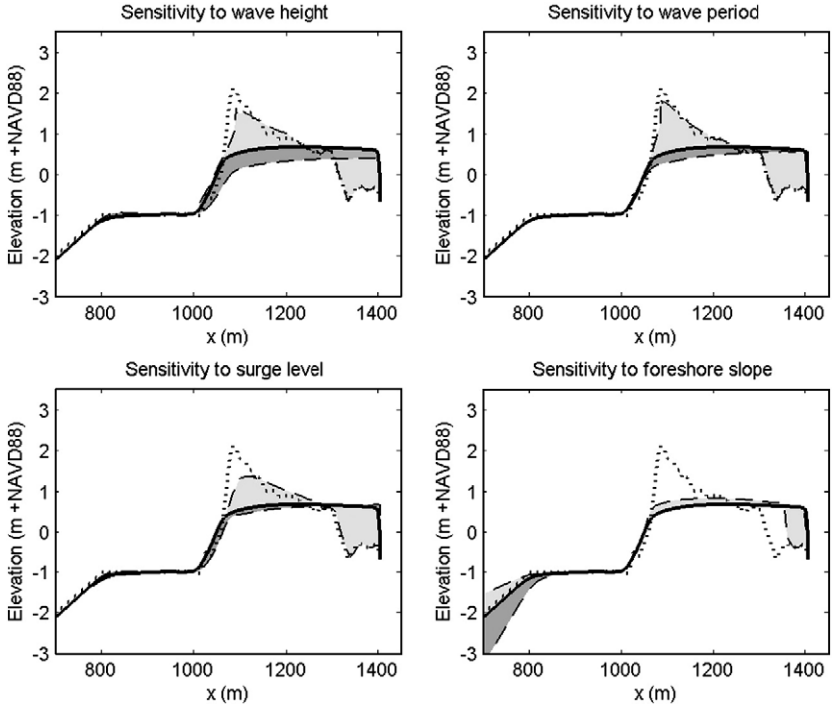

Fig. 12. Sensitivity of profile A to the incident wave height (top left panel), wave period (top right panel), surge level (bottom left panel) and foreshore slope (bottom right panel). The initial (dotted line) and final profile (solid line) of the base simulation are shown in all four panels. The difference between the final profile of the sensitivity simulation and the base simulation is shown in light grey (for cases S2, S4, S6 and S8) or dark grey (for cases S1, S3, S5 and S7).

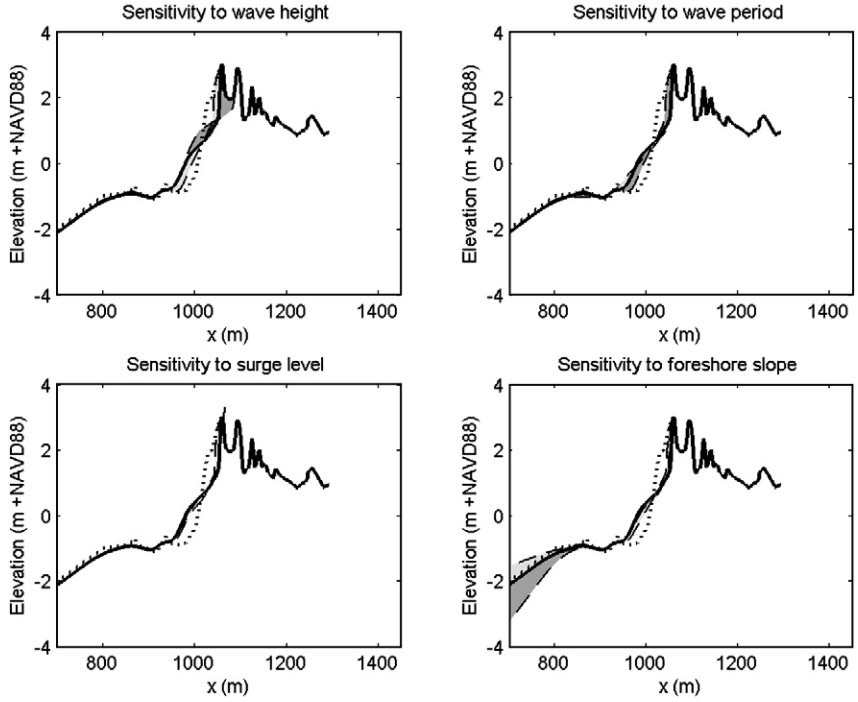

Fig. 13. Sensitivity of profile C to the incident wave height (top left panel), wave period (top right panel), surge level (bottom left panel) and foreshore slope (bottom right panel). The initial (dotted line) and final profile (solid line) of the base simulation are shown in all four panels. The difference between the final profile of the sensitivity simulation and the base simulation is shown in light grey (for cases S2, S4, S6 and S8) or dark grey (for cases S1, S3, S5 and S7).

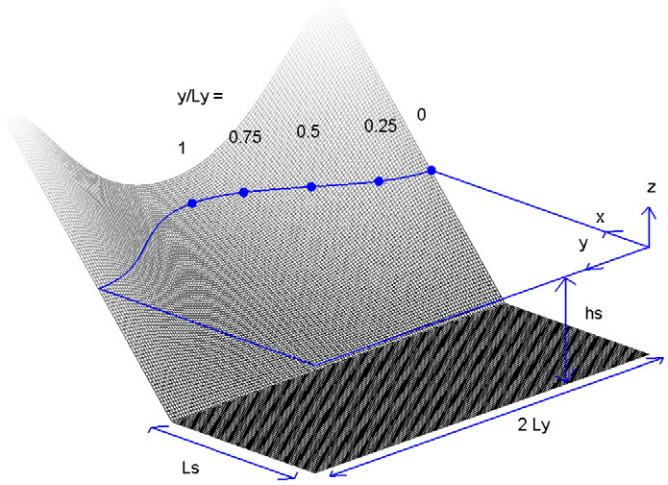

Fig. 14. Definition sketch of the concave beach bathymetry (courtesy of H.T. Özkan-Haller).

solitary wave on a concave bay with a sloping bottom (Fig. 12) that was obtained by Özkan-Haller and Kirby (1997), who used a Fourier–Chebyshev Collocation model of the nonlinear non-dispersive shallow water equations. This solution is used rather than the original simulation by Zelt (1986), who used a fully Lagrangian finite element model of the shallow water equations, which included some dissipative and dispersive terms which presently cannot be modelled in XBeach. The XBeach model is run without friction, short-wave forcing or diffusion.

Fig. 14 shows the definition sketch of the concave beach bathymetry in the present coordinate system, converted from the original system by Zelt (1986). The bathymetry consists of a flat bottom part and a beach part with a sinusoidally varying slope. For Zelt's (1986) fixed parameter choice of $h_s/L_y = 4/(10\pi)$, the bathymetry is given by

$$h = \begin{cases} h_s & ,x \le L_s \\ h_s - \dfrac{0.4(x-L_s)}{3-\cos\left(\dfrac{\pi y}{L_y}\right)} & ,x > L_s \end{cases} \tag{0.36}$$

where h_s is the shelf depth, L_s is the length of the shelf in the modelled domain and L_y is the length scale of the longshore variation of the beach. This results in a beach slope $h_x = 0.1$ in the center of the bay and of $h_x = 0.2$ normal to the "headlands". In the following we chose $L_y = 8$ m, which determines $h_s = 1.0182$ m. We set $L_s = L_y$ and different values for L_s only cause phase shifts in the results, but no qualitative difference, so this parameter is not important in this problem. Also indicated in the figure are the five stations where the vertical runup (the surface elevation at the shoreline) will be measured.

At the offshore $x = 0$ boundary we specify an incoming solitary wave, which in dimensional form reads

$$z_s = \alpha h_s \sec h^2\left(\sqrt{\frac{3g}{4h_s}\alpha(1+\alpha)}(t-t_0)\right) \tag{0.37}$$

which is similar to Zelt's (1986) Eq. (5.3.7) except that we neglect the arbitrary phase shift. The phase shift t_0 is chosen such that the surface elevation of the solitary wave at $t = 0$ is 1% of the maximum amplitude. The only parameter yet to be chosen is α. We will compare our model to Zelt's case of $\alpha = \frac{H}{h_s} = 0.02$ where H is the offshore wave height. Zelt found that the wave broke for a value of $\alpha = 0.03$, so the present test should involve no breaking, but has a large enough nonlinearity to exhibit a pronounce two-dimensional runup.

Any outgoing waves will be absorbed at the offshore boundary by the absorbing–generating boundary condition. At the lateral boundaries $y = 0$ and $y = 2\,L_s$ we specify a no-flux (wall) boundary condition

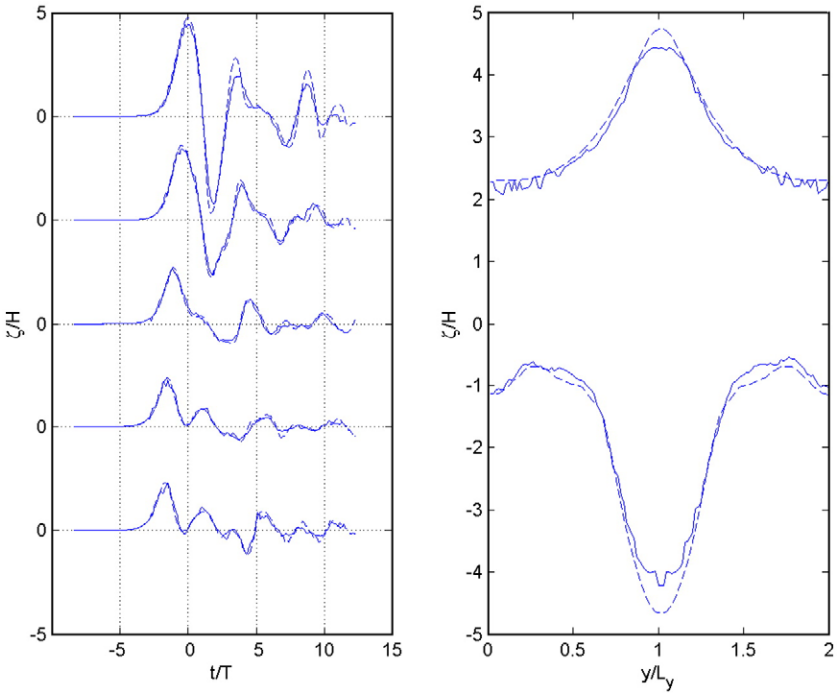

Fig. 15. Comparison of present model (solid) to Özkan-Haller and Kirby (1997) (dashed): (a) time series of runup in 5 stations from top to bottom $y/L_y = 1$, 0.75, 0.5, 0.25 and 0 respectively, and (b) maximum runup and rundown.

following Zelt. The numerical parameters are $\Delta x = \Delta y = 0.125$ m with a Courant number of 0.7.

Fig. 15a shows the vertical runup ζ normalized with the offshore wave height H as a function of time, which is normalized by $T = \sqrt{gh_s}/L_y$ at the 5 cross-sections indicated in Fig. 14. The solid lines represent the present model results while the dashed lines denote Őzkan-Haller and Kirby's (1997) numerical results. We see that the agreement is generally good, except that the present model does not capture the second peak in the time series at $y/L_y = 1$ very well. This secondary peak or "ringing" is due to the wave energy that is trapped along the coast and propagates towards the midpoint of the bay (Zelt, 1986). It is suspected that this focusing mechanism is not properly captured, because the present method approximates the shoreline as a staircase pattern, which in effect lengthens the shoreline. Also, the spatial derivatives are not evaluated parallel and perpendicular to the actual shoreline but in the fixed x and y directions. The agreement at locations $y/L_y = 0.25$, $y/L_y = 0$ 0.5 and $y/L_y = 0.75$ is generally good despite the large gradient of the local shoreline relative to our grid. The statistical overall score for the time series is $R^2 = 0.986$, SCI = 0.170 and the relative bias = 0.009.

Note that Őzkan-Haller and Kirby (1997) use a moving, adapting grid with a fixed Δy (which is equal to the present model's Δy in this comparison) but with a spatially and temporally varying Δx so that the grid spacing near the shoreline is very small. In the present model Δx is set equal to Δy, which means that we can expect to have less resolution at the shoreline than Őzkan-Haller and Kirby (1997).

Fig. 15b shows the maximum vertical runup and rundown, normalized by H, versus the alongshore coordinate y. It is seen that the maximum runup agrees well with Őzkan-Haller and Kirby (1997) but that the maximum rundown is not represented well in the center of the domain. The 'wiggles' in the solid line are evidence of the staircasing of the shoreline: since the shoreline is not treated as a continuous but rather as a discrete function, so is the runup in the individual nodes. The statistical score for the maximum runup is $R^2 = 0.98$, SCI = 0.04 and the relative bias = −0.03.

The above results are consistent with the results obtained with the SHORECIRC model which is based on similar hydrodynamic equations, see Van Dongeren and Svendsen (1997b), and show that also the current model is capable of representing runup and rundown.

4.5. Delilah

In order to verify the 2DH hydrodynamics of XBeach forced by directionally-spread short waves a simulation is set up to compare model results to field measurements. In this case the Delilah field experiment at Duck, North Carolina is selected as a suitable test location. The period that is modelled is October 13th 1990, which was a stormy day, between 16:00 and 17:00 h. The significant wave height at 8 m water depth was 1.81 m, with a peak period of 10.8 s and a mean angle of incidence of −16° relative to the shoreward normal. This period is selected because the wave conditions are energetic enough to generate a significant infragravity wave component and the incident wave spectrum is sufficiently narrow-banded to justify the assumptions in the model boundary conditions. The model is forced with the wave spectrum measured at 8 m water depth (Birkemeier et al., 1997). A measured tidal signal is imposed on the model boundaries of which the mean level is 0.69 m above datum. The slope of the wave front in the roller model β is set to the default value of 0.10. A constant grid size of 5 m in cross-shore and 10 m in longshore direction is used. The resolution of the wave model in directional space is 15°. The model is set to generate output at the location of the primary cross-shore measurement array, gauge numbers 10, 20, 30, 40, 50, 60, 70, 80 and 90 (Fig. 16).

The modelled time-averaged wave heights of the short waves are compared to the time-averaged wave heights measured at the gauges. These results are shown in the first panel of Fig. 17. Unfortunately, no data exist for gauge number 60.

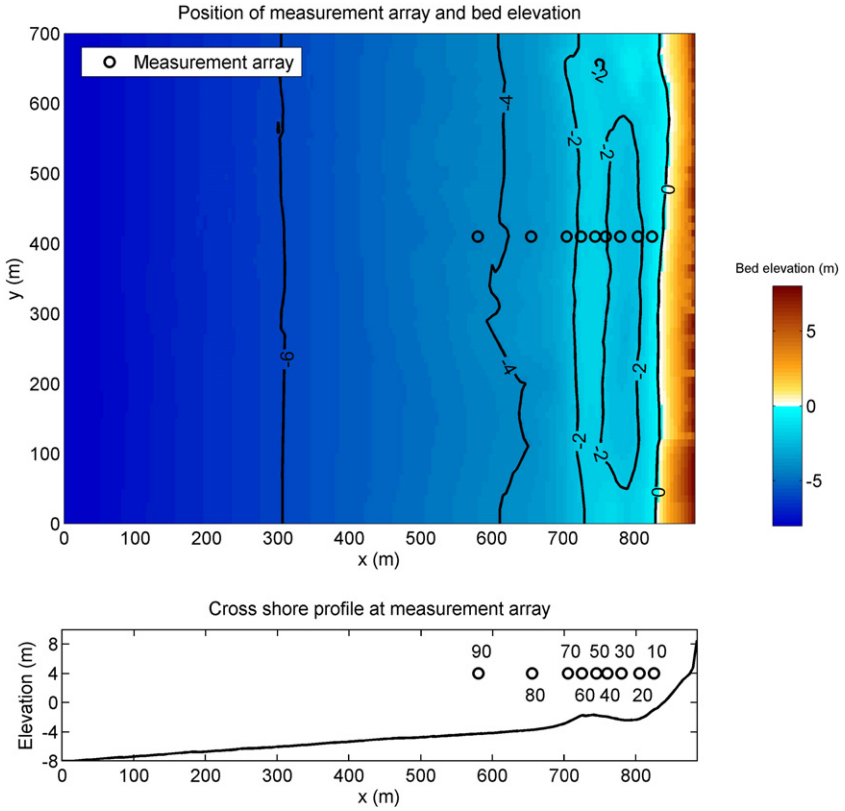

Fig. 16. Delilah field experiment 1990. Top panel: plan view of the model location and measurement gauge array (circles). Bottom panel: cross-shore profile at the location of the measurement gauge array (circles) and measurement gauge names.

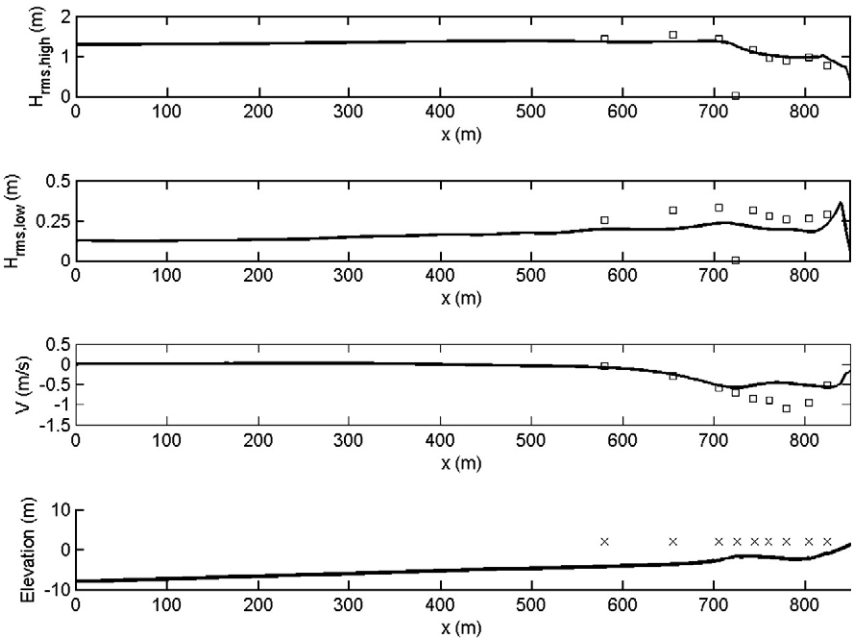

Fig. 17. Delilah 1990: First panel: time-averaged measured (squares) and modelled (line) RMS-wave height of the short waves. Second panel: time-averaged measured (squares) and modelled (line) RMS-wave height of the infragravity waves. Third panel: time-averaged measured (squares) and modelled (line) longshore velocity. Fourth panel: cross-shore profile at the location of the measurement gauge array with the positions of the gauges (crosses).

The infragravity wave height is calculated as follows (van Dongeren et al., 2003):

$$H_{\mathrm{rms,low}} = \sqrt{8 \int_{0.005\,\mathrm{Hz}}^{0.05\,\mathrm{Hz}} Sdf} \tag{0.38}$$

As can be seen in the second panel of Fig. 17, the XBeach model underestimates the infragravity wave height, but does follow the measured cross-shore trend well.

The measured and modelled time-averaged longshore current is shown in the third panel of Fig. 17. It can be seen that the model strongly underpredicts the longshore current in the trench between

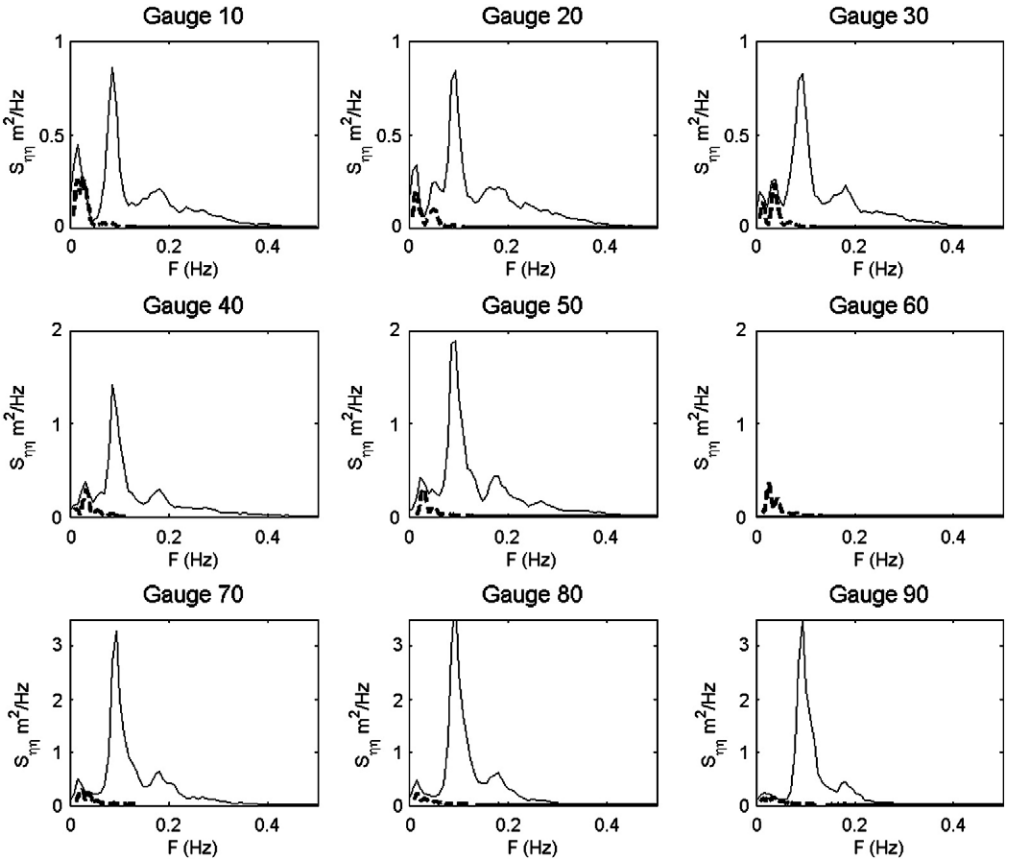

Fig. 18. Delilah 1990: Measured (solid line) and modelled (dashed line) surface elevation spectra for nine locations in the primary cross-shore array. Gauge 90 is the most seaward.

measurement gauge 60 and the shore. Further calibration of the short wave and roller parameters is required in order to improve the simulated longshore current in this trough. The correlation coefficient, scatter index, relative bias and Brier Skill Score for the simulation are shown in Table 5. Results are somewhat sensitive to the choice of roller parameter β.

The modelled and measured sea surface elevation spectra at all nine gauge locations are shown in Fig. 18. Note that similar to Fig. 8 the modelled surface elevation spectra only contain low-frequency components associated with wave groups. The figure shows a migration of energy from high to low frequencies in shoreward direction in the measured spectra. The simulated spectra reproduce well the trend of increasing energy in the low-frequency band in shoreward direction, but the amount of energy in the simulated low-frequency band is less than in the measurements. In conclusion it can be stated that the model reproduces to a high degree of accuracy the short-wave transformation in the shoaling and breaker zone. The transfer of energy from high to low frequencies in the model has qualitative skill. The longshore velocity in the nearshore requires additional calibration of the short wave and roller parameters.

4.6. ZWIN breaching test (Visser, 1998)

Having examined two-dimensional hydrodynamics, we move to 2D morphodynamics. The next test carried out is that on the Zwin breach growth experiment, as reported by Visser (1998). In the mouth of the Zwin, a tidal inlet located at the border between the Netherlands and Belgium, an artificial dam was constructed with a crest height of 3.3 m + N.A.P. (Dutch datum, approx. MSL), crest width 8 m, inner slope 1:3 outer slope 1:1.6 and length 250 m. An initial depression of 0.8 m was made in the middle of the dam having a width of 1 m and a side-slope of 1:1.6 to ensure that the breach initiated at this location. The level of the surrounding sea bed was about 0.7 m + N.A.P. The mean tidal prism of the Zwin is about 350,000 m^3. The polder area A_p as a function of the water level behind the dam z_s is given by:

$$\begin{aligned} A_p &= (170,000\,\mathrm{m})z_s - 100,000\,\mathrm{m}^2, 0.60\,\mathrm{m} < z_s < 2.3\,\mathrm{m} + N.A.P. \\ A_p &= (2,100,000\,\mathrm{m})z_s - 4,540,000\,\mathrm{m}^2, \quad z_s \geq 2.3\,\mathrm{m} + N.A.P. \end{aligned} \tag{0.39}$$

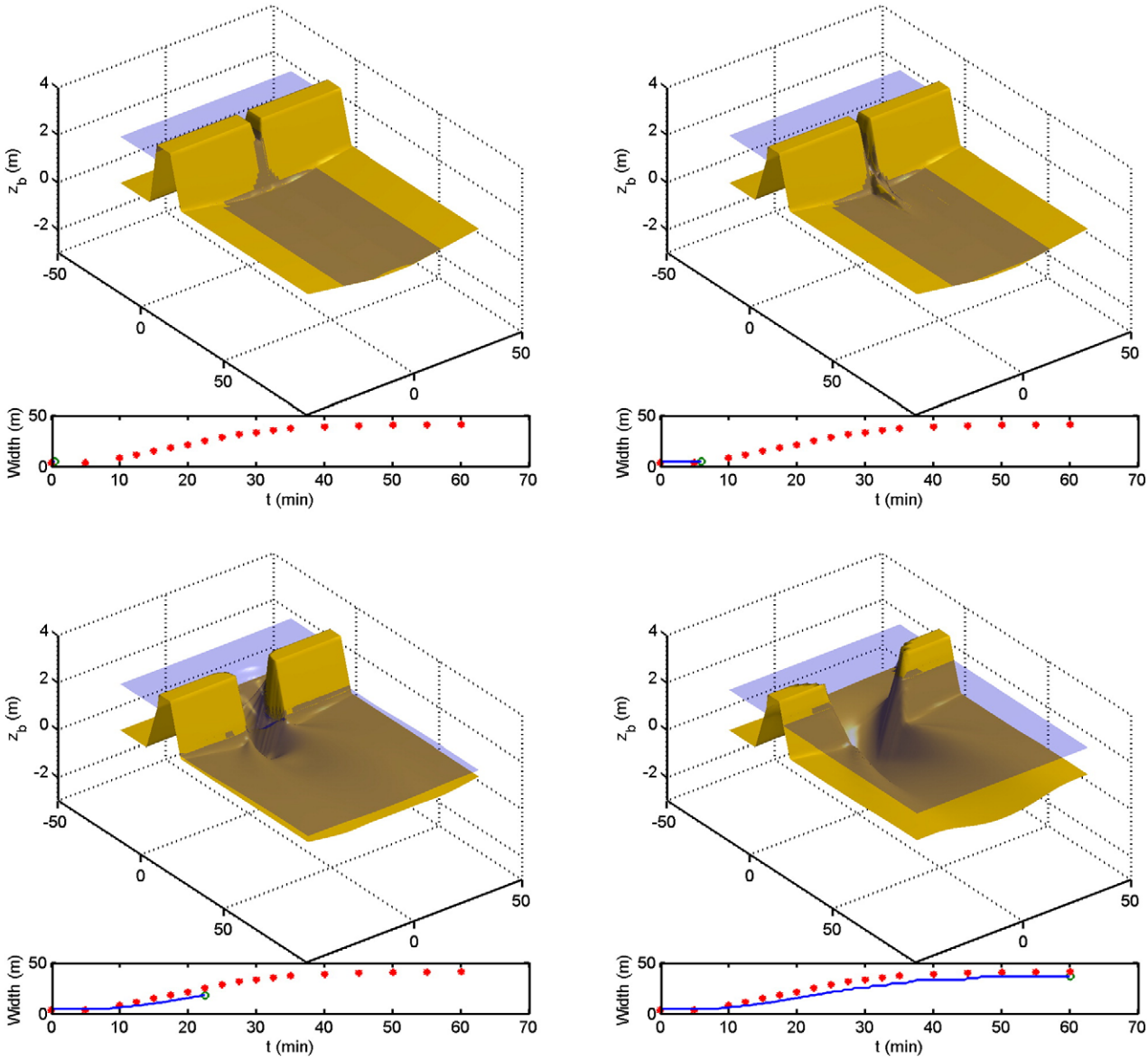

Fig. 19. Sequence of 3D visualizations of the breach during the Zwin test (Visser, 1998). Bed level, water level and development of breach width (dots: observation, line: model).

At $t=0$, about 10 min prior to high water, the water level at the seaside was NAP + 2.72 m. At $t=10$ min a water level of 2.75 m + N.A.P. was reached. For the remainder of the test, which had a total duration of 1 h, the water level marginally decreased. After 1 the breach growth became nil, as the water level of the polder area behind the breached equaled the sea level. The wave height near the dam was negligible during the experiment. The wind speed was about 2 m/s.

Until $t=6.5$ min the breach depth grew whereas the breach width remained constant. At $t=6.5$ min the original dike structure had nearly completely disappeared over the initial depression width of 1 m. Near $t=6.5$ min the onset of lateral breach growth was observed. The scour hole developed further down to a depth of 1.6 m–N.A.P. (4.9 m below the original dam crest level). The rate of lateral breach growth was about 2 cm/s. After approximately 40 min the process slowed down considerably and after approximately 1 h the water levels at both sides were equal.

A schematized representation of the Zwin test was created in XBeach, with at the sea side a uniform bed level at 0.7 m + NAP, and inside the basin a prismatic profile with the deepest point at 0.7 m + NAP and sloping sides, such that the polder area as a function of the water level was in accordance with Eq. (0.39). The grid is non-equidistant with grid sizes gradually varying from 0.5 m near the breach to approx. 50 m far away from it. The median grain diameter D_{50} of the bed material was set to 0.3 mm in accordance with the prototype test conditions for the artificial dam. The applied critical slopes for avalanching are the same as in other tests and standard settings were applied for the transport formulations (see Appendix A for default model settings). Waves were negligible in the test and were set to zero. The model was run with a CFL of 0.5 and remained smooth and stable despite the steep slopes and supercritical flows.

In Fig. 19 a sequence of 3D images is shown depicting the various stages in the breaching process: the initial overflowing, the cutting back of the breach, the deepening and finally the widening of the breach. Qualitatively and quantitatively the results are in agreement with the experiment by Visser (1998), although details may be different due to the schematized initial bathymetry.

In Fig. 20 a comparison is given between measured and simulated water levels, flow velocities and development of the breach width in time. Observation point MS2 is 30 m upstream of the center point of the breach and MS4 is 30 m downstream of it. In MS4 there was some ambiguity in the measured initial water level, which explains the initial discrepancy between measurements and simulations. The slight reduction in water level at the end of the measurement in MS2 is due to a rather narrow channel that was present in reality but not in the model, which causes higher velocities than in our model and a reduction of the mean water surface. In spite of these differences, the overall agreement for the development of the velocity in MS4 and for the breach widening is quite satisfactory. Measured and simulated flow velocities compare reasonably well in MS4.

Table 4
Error statistics for breach width development during the Sensitivity runs of the Zwin test.

Run	Description	R^2	SCI	Rel. bias
r00	Default settings	0.94	0.09	−0.06
r01	No bed-slope effect	0.88	0.44	−0.39
r02	Chezy = 50 √m/s instead of 65 √m/s	0.94	0.19	−0.16
r03	Dryslp = 0.6 instead of 1	0.93	0.19	−0.17
r04	Wetslp = 0.15 instead of 0.3	0.92	0.86	0.81
r05	D_{50} = 0.2 mm instead of 0.3 mm	0.94	0.10	0.01
r06	Adaptation timescale = 0.2 s instead of 0.1 s	0.94	0.28	−0.23

A number of sensitivity runs were carried out to see if the presented simulation fits within a range of sensible model outcomes. The breach width development and statistical errors are shown in Fig. 20 and Table 4 respectively. Qualitatively, the evolution is similar in all cases; the main differences are in the rate of breaching and (for reduced wet critical slope) the final slopes. The breaching process is somewhat faster for a reduced D_{50}, and much too fast for a reduced critical wet slope of 0.15, leading to a large positive bias. Excluding the bed-slope effect, increasing the roughness (reducing Chezy) and increasing the adaptation timescale for suspended sediment all lead to a moderate reduction in the speed of the breaching process, as expected. Somewhat counter-intuitively, a reduction in dry critical slope leads to a (modest) reduction in the breach widening rate; this can be explained by the fact that early on in the process the breach is clogged up by sediment from the dry part of the dike. The overall conclusion of the sensitivity tests is that the model performs robustly and is not overly sensitive to changes in input parameters.

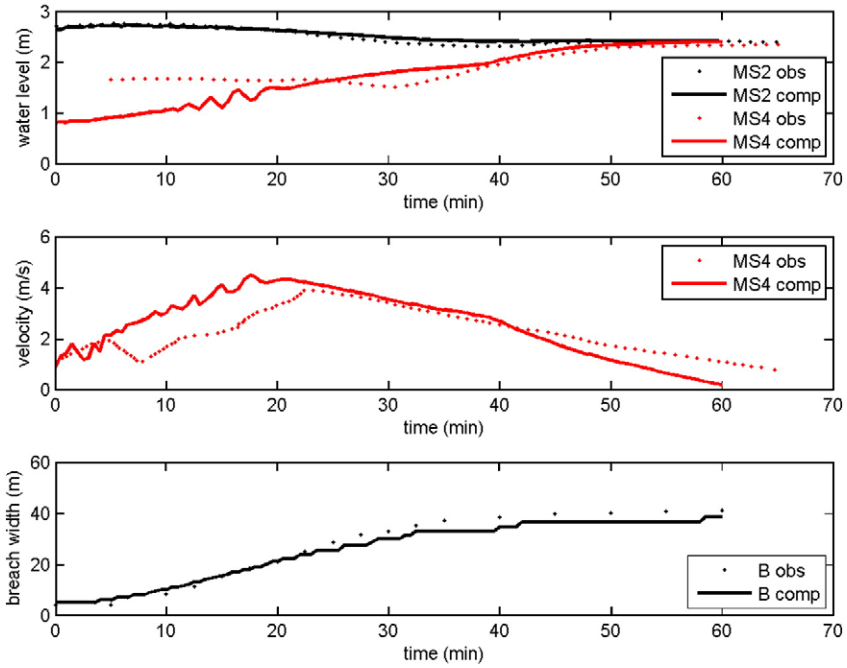

Fig. 20. Zwin test (Visser, 1998). Observed (drawn lines) and modelled (dashed lines) time series of water level (top panel and velocity (middle panel). Bottom panel: development of breach width, observations (dots) vs. model (drawn line).

5. Summary and conclusions

A robust and physics-based public-domain model has been developed with which the various stages in hurricane impacts on barrier coasts can be modelled seamlessly. The potential of the model strategy has been shown in a number of analytical, lab and field cases. These cases cover a range of functionalities and are shown to be represented quite well with a standard set of model parameters. The statistical scores for each of the test cases, according to the definitions of the scores in Table 1 are given below (Table 5).

In the LIP11D-2E test case, it was shown that the model can simulate dune erosion from both avalanching and infragravity motions without extensive extrapolations from the wet domain to the dune top. Also it was shown that in physical model tests, the type of wave generation (first order or second order) can have a significant effect on infragravity waves throughout the flume and thereby on the rate of dune erosion, in the specific case leading to an overestimation of erosion volumes by 10–15%.

The more recent test case of Deltaflume 2006 shows the model's capability to deal with more complex profiles and second-order wave generation, and clearly illustrates the dominance of infragravity wave motions in the swash zone, of which spectra and even time series are well reproduced by the model. Time-averaged hydrodynamic parameters are generally predicted with a scatter index and a relative bias of less than 10%, with the exception of the depth- and time-averaged current.

In a field case, a qualitative comparison was carried out for a hurricane at Assateague Island and generally showed the correct trends for profiles that responded quite differently, ranging from dune erosion to overwashing.

The long-wave runup was tested against 1D and 2DH analytical cases; since the 2DH case requires a correct behaviour for 1D, only the 2DH case is described in detail here. The model exhibits the correct behaviour and reproduces the analytical solutions within the accuracy that can be expected for the applied grid resolution.

Validation of the hydrodynamics of the model against Delilah measurements shows that both incident and infragravity band waves are modelled accurately in a realistic field case, especially in the inner surf zone. The prediction of longshore velocity is sensitive to the choice of roller parameter β, with $\beta=0.05$ giving slightly better results for this case than the default case of $\beta=0.10$.

Table 5
Summary of error statistics.

Test case	Parameter	R^2	SCI	Rel. bias	BSS
Lip11d-2E	$H_{rms,HI}$	0.88	0.07	−0.03	
	$H_{rms,LO}$	0.82	0.08	0.02	
	$U_{rms,HI}$	0.44	0.11	0.08	
	$U_{rms,LO}$	0.88	0.08	0.02	
	U_{mean}	0.34	0.44	−0.28	
	Sed/Ero	0.85	0.55	−0.14	0.72
	Erosion volume	0.87	0.06	−0.03	
	Dune retreat	0.83	0.08	−0.05	
Deltaflume_2005_T04	$H_{rms,HI}$	0.88	0.04	−0.003	
	$H_{rms,LO}$	0.84	0.07	0.015	
	$U_{rms,HI}$	−0.51	0.144	−0.022	
	$U_{rms,LO}$	0.82	0.09	−0.033	
	U_{mean}	0.75	0.26	0.036	
	Sed/Ero	0.97	0.162	−0.08	0.98
Zelt	Time series	0.98	0.17	0.01	
	Max runup	0.98	0.04	−0.03	
Delilah	$H_{rms,HI}$	0.852	0.093	−0.002	
	$H_{rms,LO}$	0.570	0.296	0.287	
	V ($\beta=0.10$)	0.366	0.429	0.320	
	($\beta=0.05$)	0.578	0.401	0.319	
Zwin	Breach width	0.94	0.09	−0.06	
	Max. velocity	0.76	0.36	0.16	

The Zwin test case shows that the model can qualitatively and quantitatively reproduce the breaching process in a sand dike, and that the model reacts to changes in key input parameters and settings in a predictable way.

The model presented in this paper can easily be coupled to large-scale surge and wave models such are being developed in the framework of Morphos-3D and elsewhere. All code and documentation is freely available at www.xbeach.org and is being used by a rapidly increasing user group worldwide (currently over 90 registered members). A number of studies are ongoing, among others on parallelization, on the effect of sediment sorting, on including onshore processes (e.g. skewness, asymmetry), on modelling hurricane impacts over larger 2D areas, on predicting infragravity motions on coral reefs, on modelling short-wave motions and on modelling gravel beaches.

Acknowledgements

The Research reported in this document has been made possible through the support and sponsorship of the U.S. Government through its European Research Office of the U.S. Army, under Contract no. N62558-06-C-2006, and the Office of Naval Research, in the framework of the NOPP Community Sediment Transport Model project ONR BAA 05-026, through the European Community's Seventh Framework Program under grant agreement no. 202798 (MICORE Project) and Deltares internal research fund under Strategic Research project 1200266. Permission to use data provided by the Field Research Facility of the U.S. Army Engineer Waterways Experiment Station's Coastal Engineering Research Center is appreciated.

The anonymous reviewers are thanked for their thoughtful and detailed comments.

Appendix A. Default parameter settings

Parameter	Description	Default value
Gamma	Breaker parameter in Roelvink (1993a,b) dissipation model	0.55
Alpha	Dissipation parameter in Roelvink (1993a,b) dissipation model	1.0
n	Power in breaking probability function	10
wci	Switch (0/1) to turn on wave-current interaction	0
Beta	Slope of breaking wave front in roller model	0.1
Scheme	Option to use upwind (1) or second-order Lax–Wendroff scheme (2) for short-wave energy propagation	2
hmin	Minimum depth for computation of undertow velocity	0.05 m
gammax	Maximum ratio wave height/water depth	2
hswitch	Minimum water depth considered as	0.1
Order	First-order (1) or second-order (2) wave generation	Depends on test facility or field situation
C	Chezy roughness value	65 $m^{1/2}/s$
nuh	Background horizontal viscosity	0.1 m^2/s
nuhfac	Calibration coefficient in Battjes model of horizontal viscosity	1.0
eps	Cut-off water depth for inundation	0.001 m
dico	Horizontal dispersion coefficient	1.0 m^2/s
facsl	Slope factor in sediment transport formula	1.6
Tsfac	Coefficient in adaptation time suspended sediment	0.1
wetslp	Underwater critical bed slope for avalanching	0.3
dryslp	Dry critical bed slope for avalanching	1.0
CFL	CFL number used in computation of automatic timestep	0.9

References

Andrews, D.G., McIntyre, M.E., 1978. An exact theory of nonlinear waves on a Lagrangian-mean flow. J. Fluid Mech. 89 (4), 609–646.

Arcilla, A.S., Roelvink, J.A., O'Connor, B.A., Reniers, A., Jimenez, J.A., 1994. The Delta flume '93 experiment. In: Arcilla, A.S., Kraus, N.C., Marcel, S.J.F. (Eds.), Coastal Dynamics '94: Am. Soc. of Civ. Eng., Reston, Va, pp. 488–502.

Battjes, J.A., Bakkenes, H.J., Janssen, T.T., Van Dongeren, A.R., 2004. Shoaling of subharmonic gravity waves. J. Geophys. Res. 109 (C2), C02009. doi:10.1029/2003JC001863.

Birkemeier, W.A., Donoghue, C., Long, C. E., Hathaway, K.K. and Baron, C.F. (1997) 1990 DELILAH nearshore experiment: summary report, Tech. Rep. CHL-97-4-24, Field Res. Facil., U.S. Army Corps of Eng., Waterways Exper. Stn., Vicksburg., Miss.

Damgaard, J., Dodd, N., Hall, L., Chesher, T., 2002. Morphodynamic modelling of rip channel growth. Coast. Eng. 45, 199–221.

Deigaard, R., 1993. A note on the three dimensional shear stress distribution in a surf zone. Coast. Eng. 20, 157–171.

Erikson, L., Larson, M., Hanson, H., 2005. Prediction of swash motion and run-up including the effects of swash interaction. Coast. Eng. 52, 285–302.

Feddersen, F., Guza, R.T., Elgar, S., Herbers, T.C., 2000. Velocity moments in alongshore bottom shear stress parameterizations. J. Geophys. Res. 105, 8673–8688.

Galappatti, R., Vreugdenhil, C.B., 1985. A depth integrated model for suspended transport. J. Hydraul. Res. 23 (4), 359–377.

Gallagher, E.L., Elgar, S., Guza, R.T., 1998. Observations of sand bar evolution on a natural beach. J. Geophys. Res. 90, 3203–3215.

Hasselmann, K., 1962. On the non-linear energy transfer in a gravity-wave spectrum: I. General theory. J. Fluid Mech. 12, 481–500.

Herbers, T.H.C., Elgar, S., Guza, R.T., 1994. Infragravity-frequency (0.005–0.05 Hz) motions on the shelf. Part I: forced waves. J. Phys. Oceanogr. 24 (5), 917–927.

Holthuijsen, L.H., Booij, N., Herbers, T.H.C., 1989. A prediction model for stationary short-crested waves in shallow water with ambient currents. Coast. Eng. 13, 23–54.

Huntley, D.A., Guza, R.T., Thornton, E.B., 1981. Field observations of surf beats, 1, progressive edge waves. J. Geophys. Res. 86, 6451–6466.

Jiménez, J.A., Sallenger, A.H., Fauver, L., 2006. Sediment Transport and Barrier Island Changes During Massive Overwash Events. ICCE 2006, San Diego.

Larson, M., Erikson, L., Hanson, H., 2004. An analytical model to predict dune erosion due to wave impact. Coast. Eng. 51, 675–696.

Leatherman, S.P., Williams, A.T., Fisher, J.S., 1977. Overwash sedimentation associated with a large-scale northeaster. Mar. Geol. 24, 109–121.

List, J.H., 1992. A model for two-dimensional surfbeat. J. Geophys. Res. 97, 5623–5635.

McCall, R.T. (2008), The longshore dimension in dune overwash modelling. Development, verification and validation of XBeach. MSc-thesis Delft University of Technology, the Netherlands.

Nairn, R.B., Roelvink, J.A., Southgate, H.N., 1990. Transition zone width and implications for modelling surfzone hydrodynamics. In: Edge, B.L. (Ed.), Coastal Engineering Conference, 1990: Proceedings of the International Conference: Am. Soc. Of Civ. Eng., Reston, Va, pp. 68–81.

Nishi, R., Kraus, N.C., 1996. Mechanism and calculation of sand dune erosion by storms. Proceedings of the 25th Coastal Engineering Conference. ASCE, pp. 3034–3047.

Overton, M.F., Fisher, J.S., 1988. Laboratory investigation of dune erosion. J. Waterw. Port Coast. Ocean Eng. 114 (3), 367–373.

Özkan-Haller, H.T., Kirby, J.T., 1997. A Fourier–Chebyshev collocation method for the shallow water equations including shoreline runup. Appl. Ocean Res. 19, 21–34.

Phillips, O.M., 1977. The Dynamics of the Upper Ocean2nd ed. Cambridge Univ. Press, New York. 336 pp.

Raubenheimer, B., Guza, R.T., 1996. Observations and predictions of run-up. J. Geophys. Res. 101 (C10), 25,575–25,587 Nov. 15.

Reniers, A.J.H.M., Roelvink, J.A., Thornton, E.B., 2004a. Morphodynamic modelling of an embayed beach under wave group forcing. J. Geophys. Res. 109, C01030. doi:10.1029/2002JC001586.

Reniers, A.J.H.M., Thornton, E.B., Stanton, T., Roelvink, J.A., 2004b. Vertical flow structure during Sandy Duck: observations and modeling. Coast. Eng. 51 (3), 237–260 May.

Reniers, A.J.H.M., MacMahan, J., Thornton, E.B., Stanton, T.P., 2006. Modelling infragravity motions on a rip-channel beach. Coast. Eng. 53, 209–222.

Roelvink, J.A., 1993a. Dissipation in random wave groups incident on a beach. Coast. Eng. 19, 127–150.

Roelvink, J.A. (1993b), Surf beat and its effect on cross-shore profiles. Ph.D. thesis. 150 pp., Delft Univ. of Technology., Delft, Netherlands.

Roelvink, J.A., van Kessel, T., Alfageme, S., Canizares, R., 2003. Modelling of barrier island response to storms. Proc. Coastal Sediments '03, Clearwater, Florida.

Ruessink, B.G., Miles, J.R., Feddersen, F., Guza, R.T., Elgar, S., 2001. Modeling the alongshore current on barred beaches. J. Geophys. Res. 106, 22451–22463.

Sallenger, A., 2000. Storm impact scale for barrier islands. J. Coast. Res. 16 (3), 890–895.

Schaeffer, H.A., 1994. Edge waves forced by short-wave groups. J. Fluid Mech. 259, 125–148.

Soulsby, R.L., 1997. Dynamics of Marine Sands. Thomas Telford, London.

Soulsby, R.L., Hamm, L., Klopman, G., Myrhaug, D., Simons, R.R., Thomas, G.P., 1993. Wave–current interaction within and outside the bottom boundary layer. Coast. Eng. 21, 41–69.

Steetzel, H.J., 1993. Cross-shore transport during storm surges. PhD thesis Technical University Delft. ISBN 90-9006345-5, CASPARIE publishers, Zwolle.

Stelling, G.S., Duinmeijer, S.P.A., 2003. A staggered conservative scheme for every Froude number in rapidly varied shallow water flows. Int. J. Numer. Methods Fluids 43, 1329–1354.

Stive, M.J.F., de Vriend, H.J., 1994. Shear stresses and mean flow in shoaling and breaking waves. In: Edge, B.L. (Ed.), Proceedings of the Twenty-Fourth International Conference: Am. Soc. Of Civ. Eng., Reston, Va, pp. 594–608.

Stockdon, H.F., Holman, R.A., Howd, P.A., Sallenger, A.H., 2006. Empirical parameterization of setup, swash, and runup. Coast. Eng. 53, 573–588.

Svendsen, I.A., 1984. Wave heights and set-up in a surf-zone. Coast. Eng. 8, 303–329.

Thornton, E.B., MacMahan, J.H., Sallenger Jr., A.H., 2007. Rip currents, mega cusps and eroding dunes. Mar. Geol. 240, 151–167.

Tucker, M.J., 1954. Surfbeats: sea waves of 1 to 5 minutes' period. Proc. R. Soc. London, Ser. A 202, 565–573.

Van Dongeren, A.R. and Svendsenm, I.A. (1997b). Quasi 3-D modelling of nearshore hydrodynamics. Ph.D. dissertation. University of Delaware. Also: report CACR-97-04. 237 p.

Van Dongeren, A.R., Svendsen, I.A., 1997a. An absorbing–generating boundary condition for shallow water models. J. Waterw. Port Coast. Ocean Eng. 123 (6), 303–313.

Van Dongeren, A., Reniers, A., Battjes, J., Svendsen, I., 2003. Numerical modeling of infragravity wave response during DELILAH. J. Geophys. Res. 108 (C9), 3288. doi:10.1029/2002JC001332.

Van Dongeren, A., Battjes, J., Janssen, T., van Noorloos, J., Steenhauer, K., Steenbergen, G., Reniers, A., 2007. Shoaling and shoreline dissipation of low-frequency waves. J. Geophys. Res. 112, C02011. doi:10.1029/2006JC003701.

Van Gent, M.R.A., Thiel, Van, de Vries, J.S.M., Coeveld, E.M., De Vroeg, J.H., Van de Graaff, J., 2008. Large scale dune erosion tests to study the influence of the wave periods. Coast. Eng. 55 (12), 1041–1051.

Van Rijn, L.C., Walstra, D.J.R., Grasmeijer, B., Sutherland, J., Pan, S., Sierra, J.P., 2003. The predictability of cross-shore bed evolution of sandy beaches at the time scale of storms and seasons using process-based Profile models. Coast. Eng. (ISSN: 0378-3839) 47 (3), 295–327. doi:10.1016/S0378-3839(02)00120-5 January.

Van Thiel de Vries, J.S.M., van Gent, M.R.A., Walstra, D.J.R., Reniers, A.J.H.M., 2008. Analysis of dune erosion processes in large-scale flume experiments. Coast. Eng. 55 (12).

Vellinga, P., 1986. Beach and dune erosion during storm surges. PhD Thesis, Delft University of Technology.

Visser, P.J. 1998. Breach growth in sand dikes. Ph.D.-thesis Delft University of Technology, the Netherlands.

Walstra, D.J., Roelvink, J.A., Groeneweg, J., 2000. 3D calculation of wave-driven cross-shore currents. Proceedings 27th International Conference on Coastal Engineering, July 16-21, 2000, Sydney.

Wang, P., Horwitz, M.H., 2007. Erosional and depositional characteristics of regional overwash deposits caused by multiple hurricanes. Sedimentology 54, 545–564.

Zelt, J.A. (1986). "Tsunamis: the response of harbours with sloping boundaries to long wave excitation." Doctoral dissertation, Rep. No. KH-R-47, W.M. Keck Laboratory of Hydraulics and Water Resources, Division of Engineering and Applied Science, California Institute of Technology, Pasadena, CA, 318 pp.